7-2015

Numerical Simulation of Terahertz Wave Interaction with Breast Cancer Tumor Tissue Sections

Abayomi Omotola Omolewu
University of Arkansas, Fayetteville

Citation

Omolewu, A. O. (2015). Numerical Simulation of Terahertz Wave Interaction with Breast Cancer Tumor Tissue Sections. *Graduate Theses and Dissertations* Retrieved from https://scholarworks.uark.edu/etd/1186

Numerical Simulation of Terahertz Wave Interaction with Breast Cancer Tumor Tissue Sections

Numerical Simulation of Terahertz Wave Interaction with Breast Cancer Tumor Tissue Sections

A thesis submitted in partial fulfillment
of the requirements for the degree of
Master of Science in Microelectronics-Photonics

by

Abayomi Omotola Omolewu
Obafemi Awolowo University
Bachelor of Science in Engineering Physics, 2008

July 2015
University of Arkansas

This thesis is approved for recommendation to the Graduate Council.

Dr. Magda El-Shenawee
Thesis Director

Dr. Mark E. Arnold
Committee Member

Dr. Baohua Li
Committee Member

Dr. Rick Wise
Ex-Officio Member

The following signatories attest that all software used in this thesis was legally licensed for use by Abayomi O. Omolewu for research purposes and publication.

Mr. Abayomi O. Omolewu, Student	Dr. Magda El-Shenawee, Thesis Director

This thesis was submitted to http://www.turnitin.com for plagiarism review by the TurnItIn company's software. The signatories have examined the report on this thesis that was returned by TurnItIn and attest that, in their opinion, the items highlighted by the software are incidental to common usage and are not plagiarized material.

Prof. Rick Wise, Program Director	Dr. Magda El-Shenawee, Thesis Director

Abstract

This thesis presents numerical simulation of terahertz (THz) wave interaction with breast cancer tumor tissue sections. The obtained results are expressed in THz images of heterogeneous material that mimics the excised breast cancer tissue sections. The finite-element software package ANSYS High Frequency Structural Simulator (HFSS) was used in this work. HFSS is a full wave frequency domain three-dimensional (3D) electromagnetic simulation package. In this work, four breast cancer tissue models based on pathology images were simulated and images of the models were obtained at 1 THz. An incident Gaussian beam was raster scanned over tissue model configurations and the reflected electric fields were calculated at a grid of pixels to create the images in the far and near field zones. Several parameters that influenced the accuracy of the obtained THz images were investigated. The step size used of scanning the incident Gaussian beam over the tissue model configurations was investigated. The results showed that scanning the Gaussian beam in 100 µm steps provided better images of the tissue models compared with the 200 µm step size. The simulated tissue thicknesses of 10 µm and 40 µm were investigated here to understand the challenges faced in the THz experimental results, conducted by others in the research group. The obtained results of 40 µm thick tissue model demonstrated better differentiation of the heterogeneous regions of the tissue model compared with the 10 µm thickness, which was consistent with the trend observed in the experimental results. Additional results simulating the THz camera, i.e. using a single incident Gaussians beam that illuminates the whole tissue section without raster scanning, were investigated. All simulated THz images obtained in this work are consistent with the pathology images. The results of this work helped understand the interaction of THz waves with relatively thin sections of ex vivo breast cancer tissues.

Acknowledgements

This research was supported by a grant from the Arkansas Breast Cancer Research Programs. The University of Arkansas for Medical Sciences Translational Research Institute (CSTA Grant Award # UL1TR000039) provided resources during the review and selection process.

Funding was provided by NSF/MRI award #1228958 for the purchase and maintenance of the THz system, and NSF award #1408007 for recent support.

Table of Contents

List of Figures

List of Tables

1. Introduction

1.1 Motivation

The terahertz (THz) region of the electromagnetic (EM) spectrum has received special attention in recent years and has become a rapidly growing area of research because of its numerous potential applications [1]. These applications include medical imaging, national security, non-destructive testing, material characterization and wireless communication [2]–[18]. These numerous potential applications have also led to advances in THz sources and detectors such that the THz region of the EM spectrum is no longer referred to as “THz gap” [9].

Focus has been given to the THz radiation in medical imaging because of its unique properties [19] . Unlike x-rays, which are the prevalent radiation used in medical imaging, THz radiation is non- ionizing when it interacts with biological tissue because its photons are less energetic compared to those of x-rays. THz radiation has short wavelengths, and this allows for better spatial resolution. Compared to other optical frequency, THz radiation also possesses better penetration in biological tissue [2][3].

Cancer is known to be the second most common cause of death in the US, surpassed only by death caused by heart disease [19]. This staggering statistic had driven research in THz imaging toward cancer diagnosis [2]–[6], [19]. In all these works, researchers sought to understand how terahertz systems can be used to provide better cancer diagnosis. With the great interest in cancer diagnosis, however, there have been few computational works on terahertz imaging of cancer tissue. Most of the research done has been experimental, and requires acquiring a THz time domain spectroscopy system. These THz systems are expensive, and there is need to explore other alternatives of tapping into the potential applications of the THz frequency band. One such alternative is the use of commercially available electromagnetic solvers to investigate the various application areas of the THz frequency band [20] .

There are several works that have used commercial EM solvers in exploring THz applications in electronics, and wireless communication systems [21]–[23]. However, to the best of the author's knowledge, there are no publications that have used a commercial EM solver for terahertz imaging. With a view to gaining more understanding into the imaging application of THz radiation, commercial finite element EM solver – ANSYS High Frequency Structure Simulator (HFSS) – was used to simulate experiment images obtained from a THz time domain spectroscopy system.

Extensive work had been conducted using THz time pulsed system to investigate excised breast cancer margin at the University of Arkansas. Formalin-fixed paraffin embedded flat tissue sections were imaged using the THz time-domain spectroscopy system[2], [13], [14]. This experimental work in breast cancer imaging was the major motivation to investigate THz imaging using commercial EM solver ANSYS HFSS in order to have a better understanding of how THz radiation interacts with biological tissues.

1.2 Literature Review of Terahertz Imaging

This section is aimed at reviewing some experimental THz imaging works, and this will help underscore the important role that commercial EM solvers can play in understanding THz interaction with biological tissues, especially in medical imaging.

The first demonstration of THz imaging based on THz time-domain spectroscopy was reported by Hu and Nuss of AT &T Bell laboratory in New Jersey [24]. They were able to image the metals and semiconductors that were inside a packaged integrated-circuit (IC). The metals and semiconductors in the plastic package of the IC were visible using THz imaging as shown in

Fig. 1.1. The image was created using the differences in the transmitted THz radiation through the different materials making up the IC. The outer plastic package of the IC was almost completely transparent, absorbing little of the THz radiation, and the metal part completely absorbed the THz radiation and the semiconductor part partially absorbed the radiation. These different absorbing characteristics of each material was used to create the image.

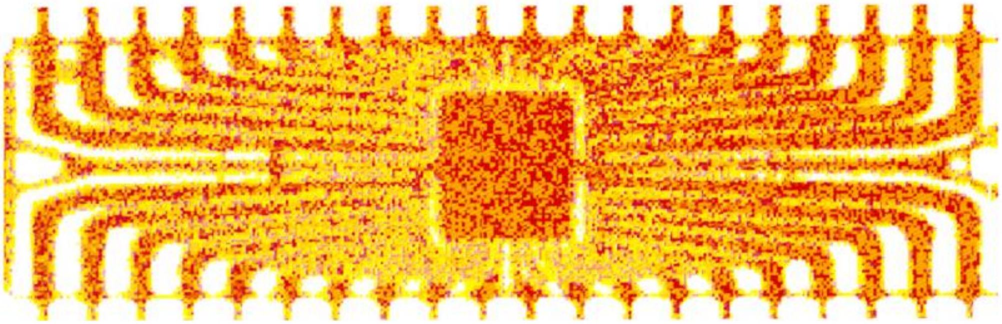

Figure 1.1: Internal structure of an integrated circuit package using THz imaging [16].

This first image spurred researchers to explore the imaging capability of the THz spectrum in application areas like national security [11], [17], [25], non-destructive testing [12], [15], [16], [25] and the area of the interest of this work, biomedical imaging [2]–[7], [10]. THz imaging has been employed in area of security to identify concealed weapons and explosives [11][17]. The insufficiency of x-ray imaging in security application has shifted focus of researchers to THz frequency. Exposure to x-rays has been a major health concern, and the inability of x-rays to detect weapon with little metal content had posed a major security threat.

Researchers not only produced a compelling image of concealed weapon like the one shown in Fig. 1.2, but also developed a technique that investigated the level of difficulty human observers experience in determining concealed weapons using THz imaging sensor [17].

Also, the work by Nobert Palka et al. developed method for getting important features of concealed materials such as explosives [11].

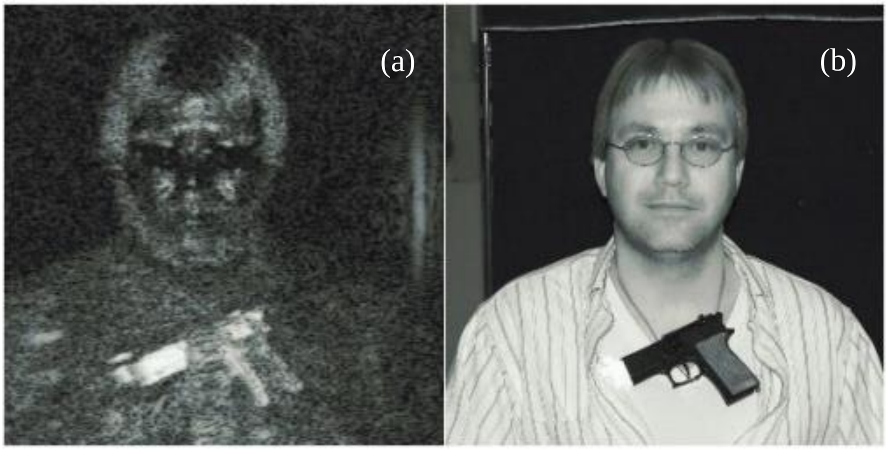

Figure 1.2: THz Image of concealed weapon. (a) THz image of a plastic gun under clothing, (b) picture showing exposed plastic gun [17].

Another area of application for THz imaging is non-destructive testing which is made possible by the availability of spectral fingerprints for different materials at THz frequency [25]. The application of THz imaging for non-destructive testing was documented in [12], where it was used to investigate the quality of plastic weld joints. Plastic weld joint probing for contaminants such as sand and air bubbles had been a challenge for the plastics industry, as most of the other methods for investigating these joints had been plagued with inefficiency and inaccuracy [12]. Researchers looked at the different deviations from the ideal weld joint in high density polyethylene (HDPE). Some of these deviations were the introduction of sand and metals into the joints. A case of partial welding was also investigated. Their result showed that the variations from the ideal wields have a different THz spectral fingerprints, and also the volume of air in the case of partial welds can be determined. THz transmission measurements done on the sample revealed good enough contrast for areas of complete weld and areas with some form of contamination along weld joints.

A non-destructive inspection of illicit drugs in mail envelopes was carried out by Kawase et al. [18]. Legal restrictions on opening private mails and the limitation of the present means of inspection of mails for drugs make THz imaging a better alternative for tackling this problem. The work successfully distinguished between three different drugs in a mail envelope as shown in Fig. 1.3a. Two of the drugs, methamphetamine (*d*- methamphetamine hydrochloride) and MDMA (*dl*-3, 4-methylenedioxymethamphetamine hydrochloride), used in the research were actual illicit drugs that are regularly abused. The third drug sample, aspirin, was used as a reference.

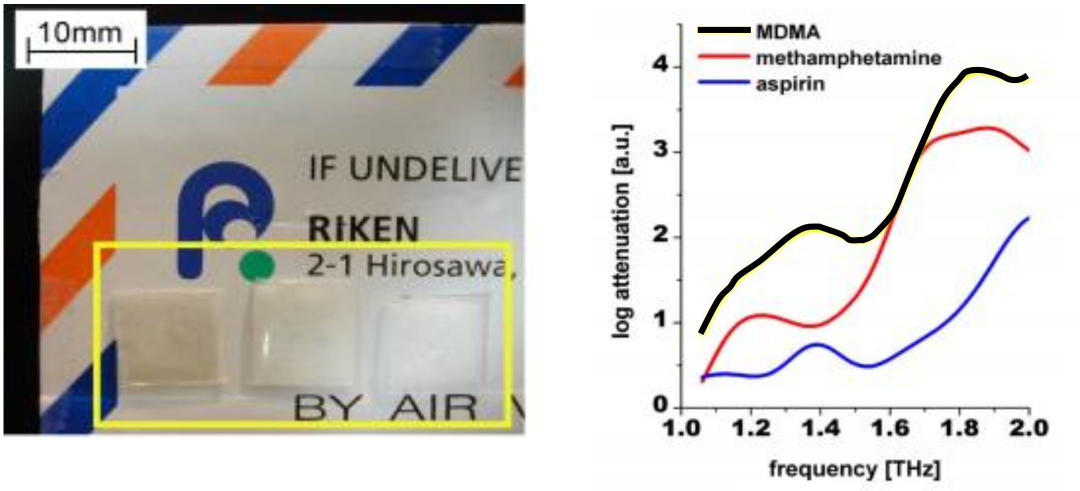

(a) (b)

Figure 1.3: Non-destructive investigation of drugs in mails. (a) Three drug samples in polyethylene, (b) absorption spectra of the drugs between 1-2.5 THz [18].

By taking transmission measurements at frequencies between 1 - 2.5 THz, absorption spectra of the three drugs were obtained as shown in Fig. 1.3b. The spectral fingerprint associated with these drugs and other chemical substances at THz frequencies make it possible to use THz imaging to identify chemicals, drugs, and explosives in mail and other packages.

THz imaging also finds application in the medical imaging due to its unique properties in interacting with biological tissues [19]. The low photon energy of the THz radiation prevents biological tissues from being damaged as a result of ionization of the tissue. This removes the worry of over-exposure that can be harmful in the case of x-rays. The sensitivity of THz radiation to water also makes it applicable in medical imaging, as difference in water content of different tissue can be used as a contrast method of identifying different tissue parts [2], [19]. Many researchers have explored this unique interaction of THz radiation with biological tissue in cancer, dentine, and eye tissue imaging.

One of the pioneering works in cancer cell imaging was by Woodward et al. [3]. Using a THz pulsed imaging system in reflection geometry, the researchers were able to differentiate between Basal Cell Carcinoma (BCC), a type of skin cancer and the normal skin tissue. Another group of researchers also worked on biological imaging application of THz radiation for breast cancer tissues [6]. They investigated the freshly excised breast cancer tissue for margins. Adequate margin of normal tissue surrounding an excised cancer tissue should be clear of cancer to avoid second surgery on patients. The margin of normal tissue around excised tissue is classified as negative if it is clear of any cancer tissue, and classified as positive if it still has cancer tissue [13]. The researchers were able to use a THz imaging system to differentiate between the normal tissue and cancer tissue in the breast, and were also able to examine the margin of fresh tissue around the excised cancer tissue. Their results agreed well with the result from histopathology examination of the excised tissue margins [6]. Other non-cancer medical imaging applications of THz radiation were recorded in literature. Crawley et al. [7], were able to get images of dental tissue and measure the thickness of the enamel. Zachary et al. [8], investigated the response of THz radiation to the water content of corneal of human eye.

Central to this research is work by Bowman et al. [2], [13], [14], where margins of formalin-fixed paraffin-embedded (FFPE) cancer tissue were investigated using a THz pulse imaging system at the University of Arkansas. Time and frequency domain images of tissue samples from patients of different ages were experimentally obtained. The THz images were compared to pathology images. Also properties of different part of the tissue were obtained. These material properties served as inputs to the computational work done in this thesis. The experimental work was carried out using the THz pulsed imaging and spectroscopy system TPS Spectra 3000 at the University of Arkansas. Images from the experimental work agreed with those obtained from histopathology. Areas of infiltrating ductal carcinoma (IDC), which is the cancerous tissue, were clearly differentiated from areas with fibro glandular (Fibro), which is the healthy tissue.

Some computational work on THz radiation interaction with biological tissue has been done by the computation electromagnetic group here at the University of Arkansas [26][27][28]. However, none of this work focused on fixed tissue section. Bowman et al. used a linear sampling method to try to investigate breast cancer margin [26]. Further work was conducted by the same group of researchers wherein discrete dipole approximation (DDSCAT) and Roytov approximation were used in creating a 2-D image of breast cancer margin [27]. Hassan et al. [28] also used linear sampling method to create images of FFPE breast cancer tissue sections that were purchased from different bio banks.

1.3 THz Pulsed Imaging and Spectroscopy System at the University

This research was based on an experimental work done using Teraview’s pulse terahertz imaging and spectroscopy system TPS Spectra 3000. The TPS Spectra 3000 is a time-domain pulsed system that uses a photoconductive switch in generating THz pulsed radiation [29]. The THz pulsed radiations are generated by exciting a biased gallium arsenide antenna with an ultrafast femtosecond laser. The THz pulse generated in this manner is broadband with frequency range typically 0.06 THz - 3 THz. The THz pulses are detected in a coherent manner using a photoconductive antenna similar to the one used in their generation. By gating the antenna with a femtosecond pulse that is synchronized to the THz radiation from the emitter, currents proportional to the THz electric fields were measured. Fig. 1.4 and Fig. 1.5 show the photo and the schematic diagram in transmission mode of THz system respectively.

Figure 1.4: Picture of the main TPS spectra 3000 at the University of Arkansas.

The TPS Spectra 3000 at the University of Arkansas has six modules: (1) the standard spectroscopy, (2) heated cell spectroscopy, (3) cryostat spectroscopy, (4) reflectance imaging module, (5) transmission imaging module, and (6) gantry system. More details of the different modules are given in the section below.

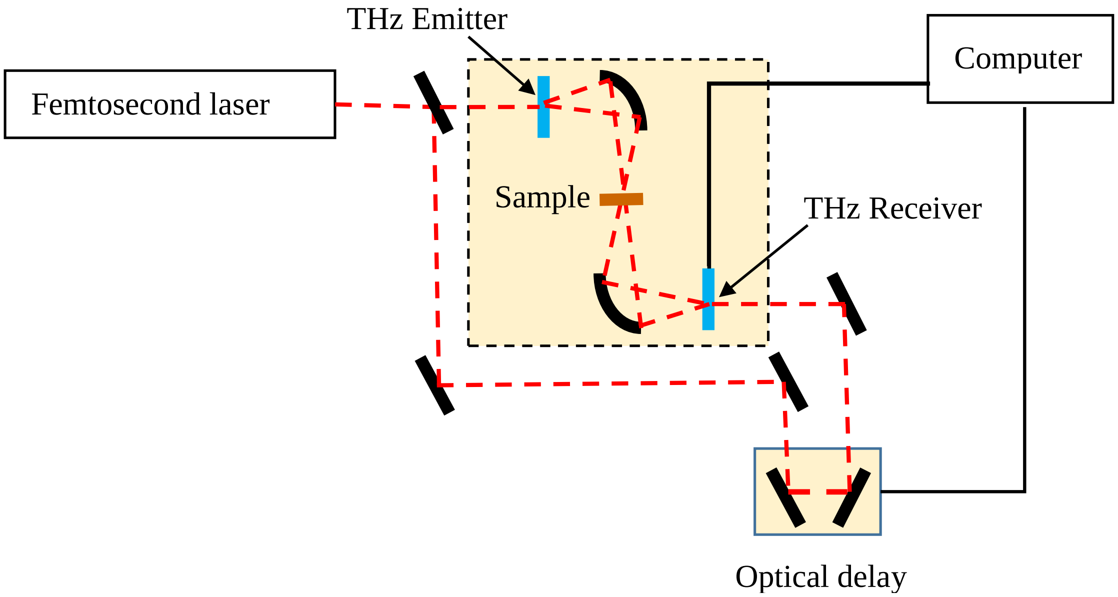

Figure 1.5: Schematic diagram of the TPS spectra 3000.

1.3.1 Standard Spectroscopy Module

Spectroscopic measurements of samples can be taken using this module at room temperature. THz beam is incident normally on a sample placed in a sample holder of the module shown in Fig. 1.6. The transmitted THz radiation from the sample is measured at the other side of the sample by a receiver.

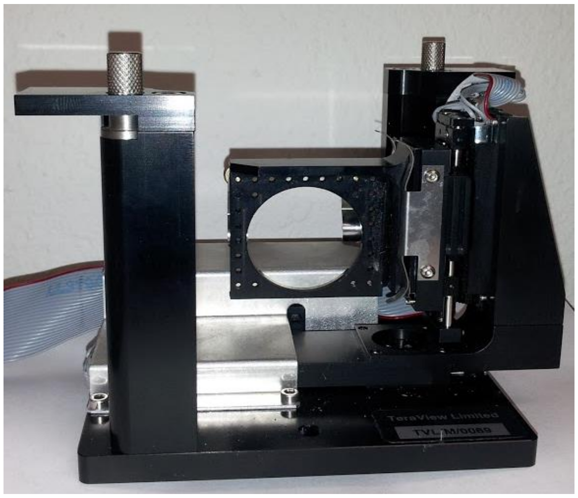

Figure 1.6: Standard spectroscopic module of TPS spectra 3000.

1.3.2 Heated Cell Spectroscopy Module

This module is used for spectroscopic measurement of both solid and liquid samples at controlled temperature. The temperatures of operation of this module range from room temperature to 573 K [29]. Fig. 1.7 shows the heat cell jacket, heater and chiller used to regulate the temperature of operation of the module.

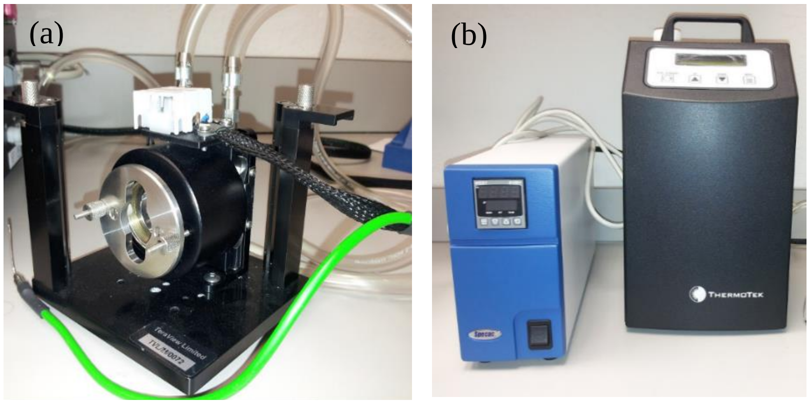

Figure 1.7: Heated cell spectroscopy module. (a) Heat cell jacket, (b) heater and chiller for temperature regulation.

1.3.3 Cryostat Spectroscopy Module

The cryostat spectroscopy module allows measurement to be done for semiconducting and condensed matter applications at very low temperature. It uses liquid helium to cool samples to temperature as low as 2.3 K [29]. The cryostat module is shown in Fig. 1.8.

1.3.4 Reflectance Imaging Module

The reflectance imaging module of the TPS Spectra 3000 is used to obtain images of samples in reflection geometry. An image of a sample is created by using THz radiation incident at an angle of 30^o to the sample and reflected radiation from the sample is measured at the receiver. The sample is raster scanned using a motorized table across the THz beam until the entire sample is imaged. 2 cm x 2 cm of sample can be imaged using the module and a penetration depth of 3 mm can be achieved [29]. Fig. 1.9 shows components of the reflectance imaging module.

Figure 1.8 Cryostat spectroscopy module.

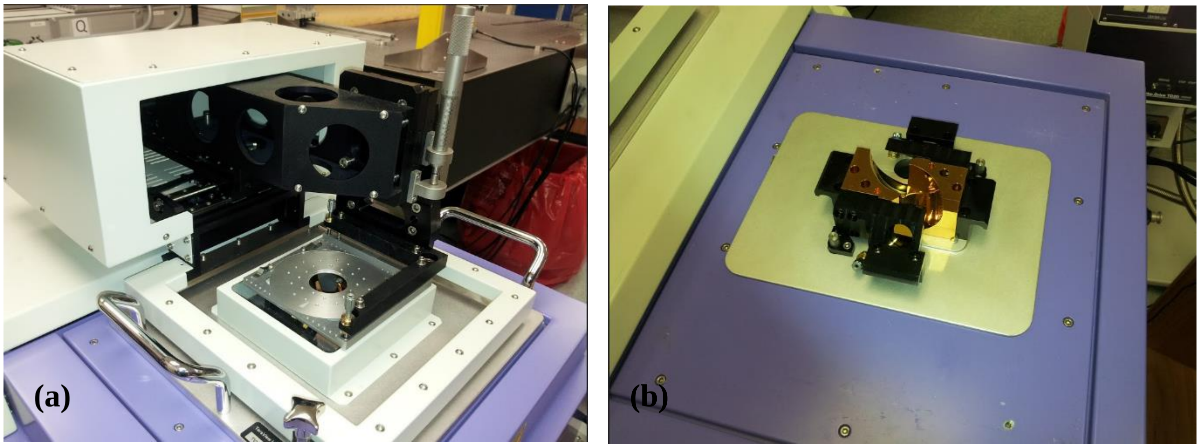

Figure 1.9: Reflection imaging module. (a) Reflection imaging module showing sample holder (b) focusing optics of the module.

1.3.5 Transmission Imaging Module

The transmission module of the system allows images of samples to be generated using the transmitted signal through the samples. The samples are also raster scanned across the THz beam using an X-Y mapper. The transmission imaging module is shown in Fig. 1.10.

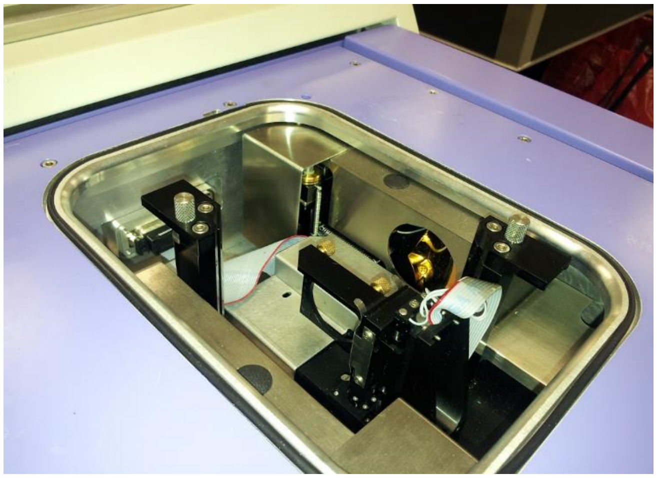

Figure 1.10: Transmission imaging module.

1.3.6 The Gantry System

The gantry system (see Fig. 1.11) is used in both reflection and transmission modes for large samples that cannot fit into the main THz system chamber. This system can be used for samples with large area up to 70 cm x 70 cm. The THz emitter and detector are attached to a gantry controlled by the system software.

Figure 1.11 TPS spectra 3000 gantry system.

The experimental work that was simulated in this research used the reflection and transmission imaging modules of the THz Spectra 3000 described in this section.

1.4 High Frequency Structural Simulator

The commercial EM solver used in this work was ANSYS High Frequency Structural Simulator (HFSS). HFSS uses different solvers based on a finite element method, an integral equation method, and other hybrid techniques [30]. This work used the 3-D full-wave electromagnetic solver based on the finite element method (FEM) for computing electromagnetic behavior in 3-D models [30]. HFSS has the capability of displaying 3-D electromagnetic field in high frequency models such as antenna, radio frequency/microwave components, and biomedical devices. Fig. 1.12 shows the electromagnetic field from an antenna on a plane simulated in HFSS.

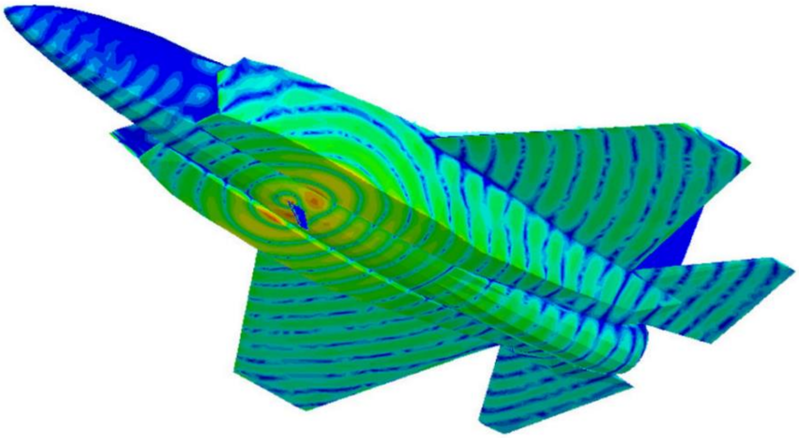

Figure 1.12: Electromagnetic field from an antenna on a plane simulated in HFSS [30].

In FEM, the computational domain is divided into small elements before field values are evaluated. The finite elements in HFSS are tetrahedra, the collection of which is referred to as a mesh. In order to solve for the field in the entire computational domain, field values at the vertices, faces, and edges of each tetrahedron are explicitly stored, while field values inside the tetrahedron are found by interpolation. Different combination of vertices, face and edge fields are used in interpolation depending on the basis function used. The second order basis function, which used field values at the vertices, faces, and edges for interpolating field values within the tetrahedral, was employed. Fig. 1.13 shows an element in HFSS, and the fields that are explicitly evaluated.

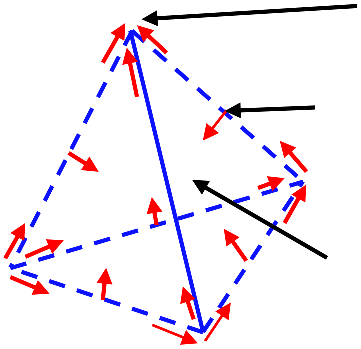

The components of a field that are tangential to the edges of an element are explicitly stored at the vertices.

The components of a field that are tangential to the edges of an element and normal to an edge are explicitly stored at midpoint of selected edges.

The value of a vector field at an interior point is interpolated from the nodal values.

Figure 1.13: A finite element in HFSS [30].

An important aspect to consider in FEM is the accuracy of the field evaluated using the method. The accuracy of field solution is dependent on the size of each finite element in a mesh. The smaller the elements making up the mesh are, the more accurate the field solutions would be. However, smaller element size results in a larger number of points where field solutions will be evaluated, which makes the solution computationally expensive. Hence, there is a tradeoff between the size of the mesh element and the field solution accuracy.

HFSS uses an iterative process called adaptive analysis to generate and appropriate mesh for a computational domain. In this process, an initial mesh is generated for the computational domain based on its geometry and the solution frequency. A solution is obtained using this initial mesh, after which the mesh is further refined in areas of high error density before another solution is obtained. This process ensures that only elements in important areas, for example around areas with excitation, are refined. The iterative adaptive solution continues until set criterion is met.

The criterion used was the maximum energy change referred to as maximum delta E (dE) per pass in HFSS. This is defined as the relative error in energy between consecutive adaptive solutions. It serves as a measure of the stability and accuracy of the field solution between consecutive passes. The value of dE approaches zero as the field solution converges.

For example, after the second iteration in an adaptive solution process, the relative change in energy, $dE_{2,}$ is evaluated as:

$$dE_2 = \frac{|E_2 - E_1|}{E_1} \qquad \text{(Equation 1.1)}$$

In general, after n iterations, the relative change in the energy, dE_n, is given as:

$$dE_n = \frac{|E_n - E_{n-1}|}{E_{n-1}} \qquad \text{(Equation 1.2)}$$

The adaptive solution process stops when the dE is below the set maximum dE in HFSS. Another way to stop the adaptive process is to enforce the maximum number of iterations. This approach is helpful when the dE is in a tolerable range after the set maximum number of passes, especially for large computational problems like the one investigated here.

1.5 Arkansas High Performance Computing Center

The simulations in this thesis are computationally large due to the terahertz frequency at which they were performed, hence more computing resources were required. The computational size of the simulation in HFSS is determined by the frequency at which the field solutions are evaluated, as the size of mesh created needs to be comparable to fraction of the wavelength. At 1

THz which is the solution frequency used in this thesis, the wavelength is 300 µm. HFSS has high performance capability (HPC) which make it run on clusters of computers, hence the simulations in the thesis were performed using the cluster of computers available at the Arkansas High Performance Computing Center (AHPCC) at the University of Arkansas [31].

The AHPCC has 5 clusters with the total compute nodes having 4,985 cores, 13.4 TB of memory, 93 TB long-term storage, 374 TB scratch storage, and 96 TB backup storage. Table 1.1 shows how these resources are distributed among the clusters.

Table 1.1: AHPCC computing resources.

Clusters	**Year Installed**	**Number of Nodes**	**Number of Core per node**	**Processor Speed**	**Memory Per Node**
Star of Arkansas	2008	157	8	2.66 GHz	16 GB
GPU	2010	6	8	2.26 GHz	12 GB
Razor I	2011	126	12	2.93 GHz	24 GB
Large Memory	2011/2012	7	32 -64	Varies	256, 512, 768GB
Razor II	2011	112	16	2.6	32 GB

1.6 Purpose and Significance of this Research

The main goal of this thesis is to validate the images experimentally obtained for breast cancer tissue using numerical simulation. In the experimental work that this research simulated, images were obtained using different tissue thicknesses: 10 µm, 20 µm, 30 µm, and 40 µm. It was observed that images from thinner sections of breast cancer tissue didn’t provide enough contrast between the different regions of the tissue when compared to thicker tissue sections. A validation of this effect of tissue thickness using simulation can help suggest an optimal thickness for imaging breast cancer tissue using THz. This will also provide better understanding of the interaction between THz radiation and breast cancer tissue. By employing this computational approach, more models with different tissue composition can also be investigated. This can add to the database of tissue fingerprints available in the THz region.

Using commercial EM solvers like HFSS provides user friendly package for investigating THz applications. The availability of material properties for biological tissue, and other materials in THz frequency range can make EM solvers convenient alternatives to experimental THz imaging systems in investigating, and understanding THz radiation for cancer applications.

2. Methodology

In this chapter, the approaches used for the HFSS computer simulations are discussed in detail. The analogy between terahertz (THz) experimental and simulation setups are identified, and justifications for choices made in the simulation are provided.

2.1 Simulation Setup

2.1.1 THz Reflection Imaging Mode

In reflection geometry, images of the samples were created from scattered THz radiation from the sample (see Fig. 2.1).

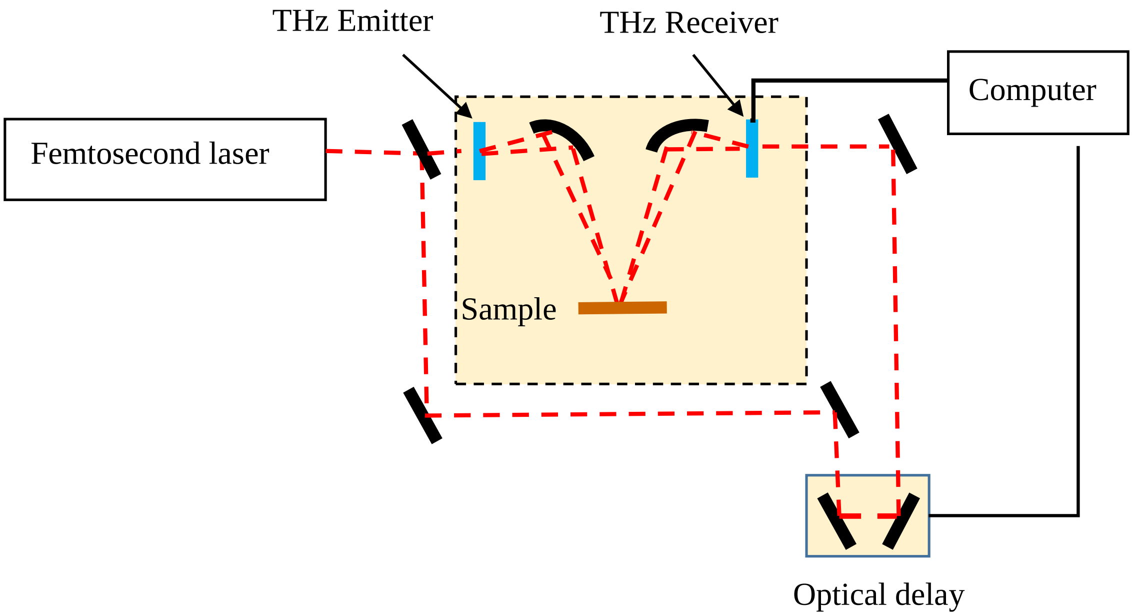

Figure 2.1: Schematic diagram of the TPS spectra 3000 in reflection geometry.

In HFSS, a model of flat tissue sample was simulated on a glass slide 1 mm thick. An initial simulation model made up of overlapping cylinders as shown in Fig. 2.2 was used to investigate the required simulation parameters. The two cylinders had circular radii of 1000 µm and heights of 10 µm. The height of the cylindrical model tissue was representative of actual breast cancer tissue thickness investigated in the experimental work [13]. A glass slide of thickness 1 mm was used in the simulation because the cancer cells were prepared on similar glass slides 1 mm thick for imaging in experimental work [13]. In the simulation, a thin sheet of perfect electric conductor (PEC) was placed under the glass to represent the silicon holder on which tissue samples were placed in the Time Domain Spectroscopy (TPS) Spectra 3000 system in reflection mode. An isometric and cross-sectional view, showing different parts of initial simulation model used for reflection imaging, are shown in Fig. 2.2 and Fig. 2.3, respectively.

The problem domain, made up of overlapping cylinders tissue model, glass, and PEC were surrounded by vacuum using perfectly matched layer (PML) boundaries. The PML boundary was used as the absorbing boundary condition because it gives a more accurate field solution compared to a radiation boundary condition in HFSS [30]. In this work, the HFSS default option for the PML layer was used with layer thickness of 1342.14 µm, conductivity of 0 S/m (Siemens/meter) and relative permittivity that has values 0.01, 1, 1.1, 0.45 depending on the direction in the PML. The problem domain and the surrounding boundaries are together referred to as the computational domain [30].

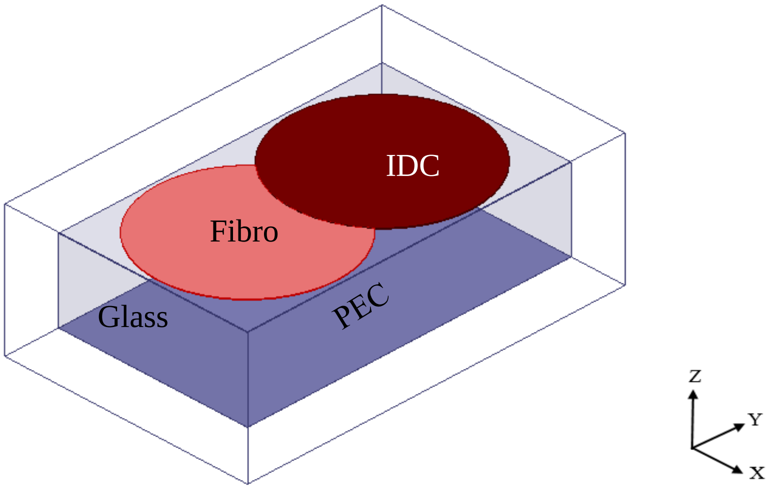

Figure 2.2: Isometric view of computational model in reflection mode.

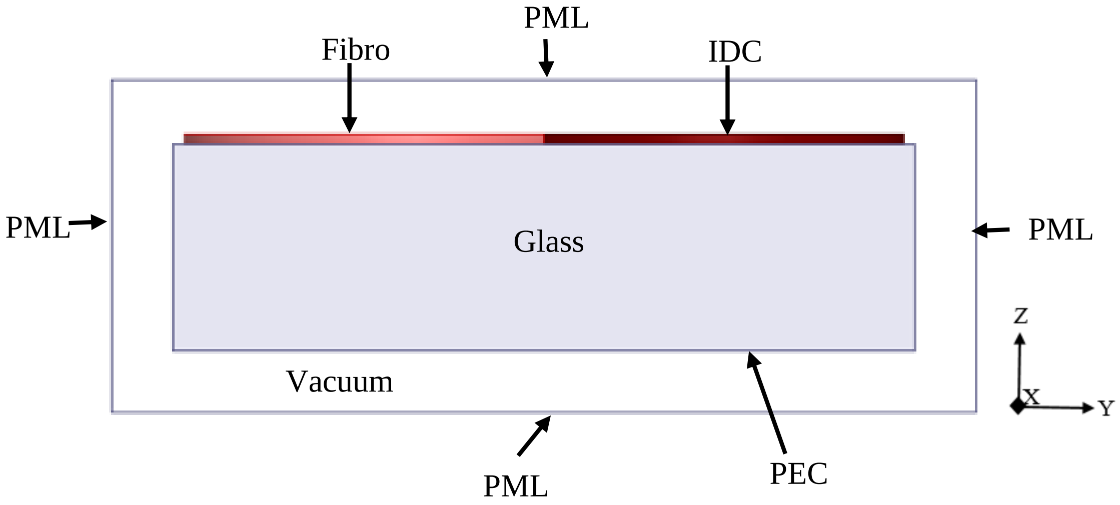

Figure 2.3: Y-Z cross-section of computational model in reflection mode.

In this work, the HFSS computer simulations were based on frequency domain solution, and a solution frequency of 1 THz was used. However, the solution at any frequency can be obtained using the same methodology. This allows for comparison between simulated images and frequency domain images obtained at 1 THz from the experimental measurements. It is important to note that the experimental THz images are based on a time domain pulse system, however the frequency domain experimental images can be obtained using the Fast Fourier Transform (FFT). The error criterion, dE, of the HFSS (discussed in Chapter 1) was *a priori* set to 0.0001, and an iterative solver was employed for the simulation.

The breast tissue properties of Fibro glandular (Fibro), Infiltrating Ductal Carcinoma (IDC), and glass at 1 THz were obtained from spectroscopic data collected from the experimental work done in [2], [13]. Table 2.1 shows the properties at 1 THz used in this work.

Table 2.1: Electrical properties of breast tissue and glass slide.

Material	**Property**	
	Relative Permittivity ε_r	**Conductivity σ (S/m)**
IDC	3.335	16.9265
Fibro	2.992	13.3248
Glass	6.5716	57.2196

In the reflection mode, the image of the tissue model was created by observing the magnitude of scattered electric field (E-field) at the PML boundary above the tissue model (see Fig. 2.3).

2.1.2 THz Transmission Imaging Mode

In transmission geometry, images of the samples are created from transmitted THz radiation through the sample (see Fig. 2.4).

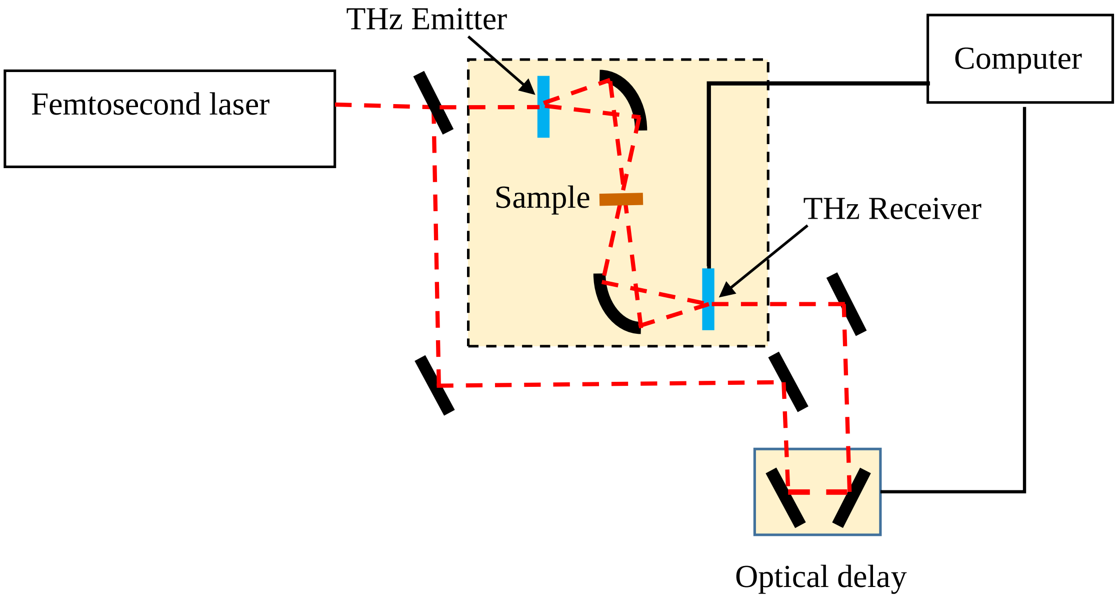

Figure 2.4: Schematic diagram of the TPS spectra 3000 in transmission geometry.

The HFSS simulation setup for the transmission imaging mode of tissue model was slightly different from reflection imaging mode. In the transmission imaging geometry, the tissue samples were placed on 1 mm thick polystyrene slides instead of glass slides, used in the reflection imaging. Glass was not used in the transmission imaging mode because it significantly attenuates the THz signal, i.e., does not allow the transmission of THz radiation through the glass slide. Polystyrene on the other hand is almost completely transparent to THz waves, allowing the THz signal to propagate through the material [14]. The transmitted THz radiation signal through the tissue-polystyrene model was used to construct the image of tissue sample in the experimental measurements [13]. In computer simulations, the images in the transmission mode were created by observing the scattered fields at the PML boundary below the polystyrene slide of the computational domain shown in isometric and cross sectional views in Fig. 2.5 and Fig. 2.6, respectively.

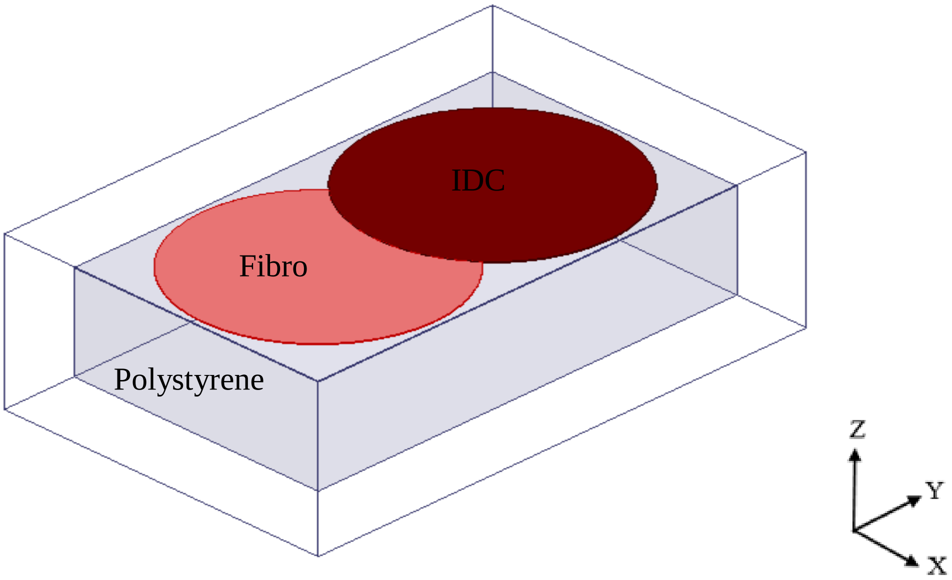

Figure 2.5: Isometric view of computational model transmission mode.

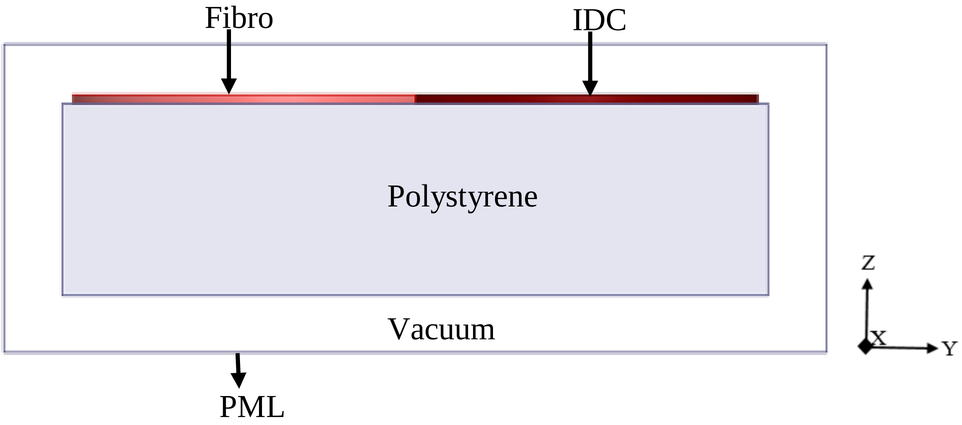

Figure 2.6: Y-Z cross section of computational model in transmission mode.

The material properties of polystyrene obtained from spectroscopic measurements are given in the Table 2.2 [13].

Table 2.2: Electrical properties of polystyrene slide.

Material	**Property**	
	Relative Permittivity ε_r	**Conductivity σ (S/m)**
Polystyrene	2.4687	0.7195

2.2 Modeling Raster Scanning in HFSS

For both reflection and transmission imaging modes of TPS Spectra 3000, images of the samples were formed by scanning the samples using a stepper motor across incident THz radiation until the entire sample had been raster scanned across the THz pulse. At each scan location on tissue, reflected or transmitted signal were recorded and used in creating an image of the sample.

In similar fashion, the Gaussian beam excitation used in the simulation was raster scanned across entire surface of the tissue model. The Gaussian beam, polarized in the x-direction and propagating in the negative z-direction, was scanned over the tissue model first in

200 µm steps, forming a 200 µm x 200 µm square grid across the entire surface of tissue model as shown in Fig. 2.7 and Fig. 2.8.

In Figure 2.8, the red dots indicate the locations where the Gaussian beam axis was located for each pixel. The reflected or transmitted E-fields for each raster location was evaluated within the square pixel around the Gaussian beam axis.

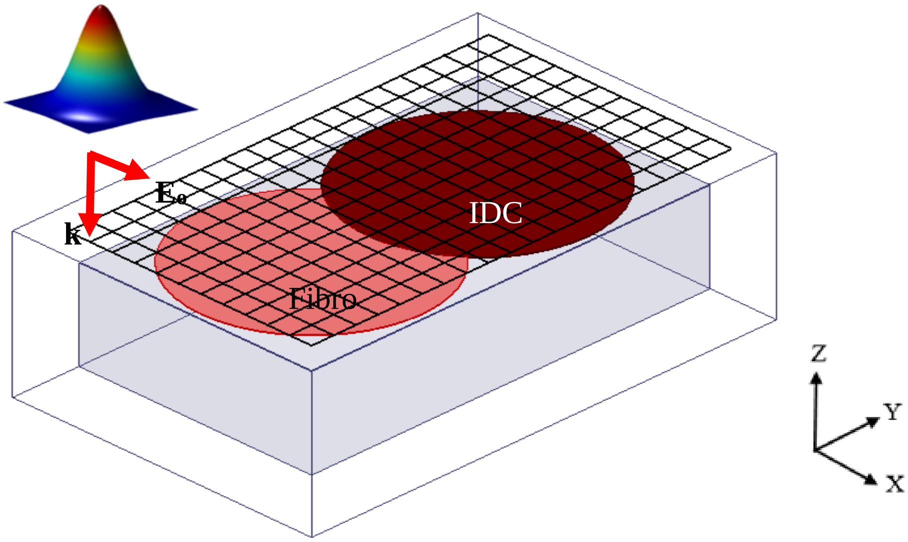

Figure 2.7: Isometric view of model showing incident Gaussian beam and pixels over tissue model.

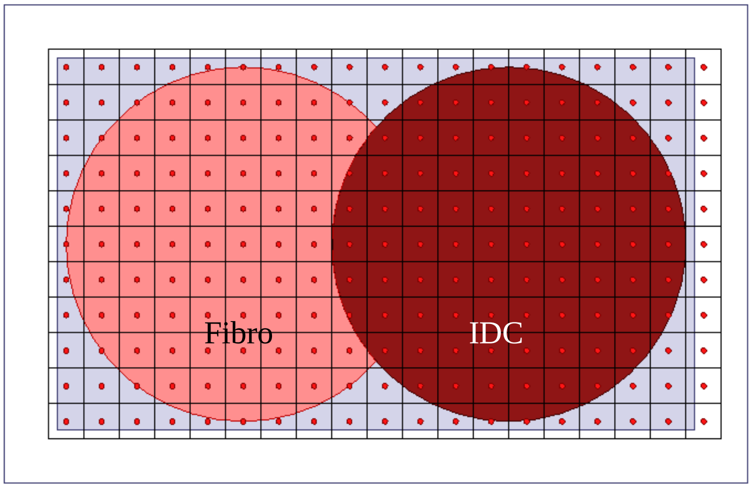

Figure 2.8: Top view of the grid showing the points where model was excited.

2.3 Convergence Approach for the HFSS Setup

In the adaptive solution method employed in HFSS, the main convergence criterion for the simulation is the dE described in section 1.4. dE represents the error between successive iterations or adaptive passes, and it is applied to the entire computational domain of the simulation. However, this simulation requires an evaluation of the scattered or transmitted E-field at each pixel for each raster scan location of the incident beam. It is possible to use a convergence approach that is local to each pixel, and this helps in reducing the computational cost and the CPU time required for solving the fields at each raster location of incident beam. This convergence approach was used here and it is described in the following subsection for the reflection imaging mode.

2.3.1 HFSS Reflection Imaging Model Convergence

The reflection imaging model described in the section 2.1 was used for investigating the convergence of the HFSS simulation. The overlapped cylinders tissue models that have radii of 1000 µm with height 10 µm on the glass slide of dimensions 1100 µm x 3600 µm x 1 mm were used (see Fig. 2.9). The overlapped cylinders tissue model was centered at the top of the glass as shown in Fig. 2.9b. Gaussian beam excitation was incident at the point of intersection of a line passing through the diameters of the cylinders and the overlapping points of the cylinders (marked by x in Fig. 2.9). Two cases of the distance between the problem domain (tissue model on glass) and surrounding PML boundary were investigated: 100 µm and 300 µm (denoted by d Fig. 2.9b).

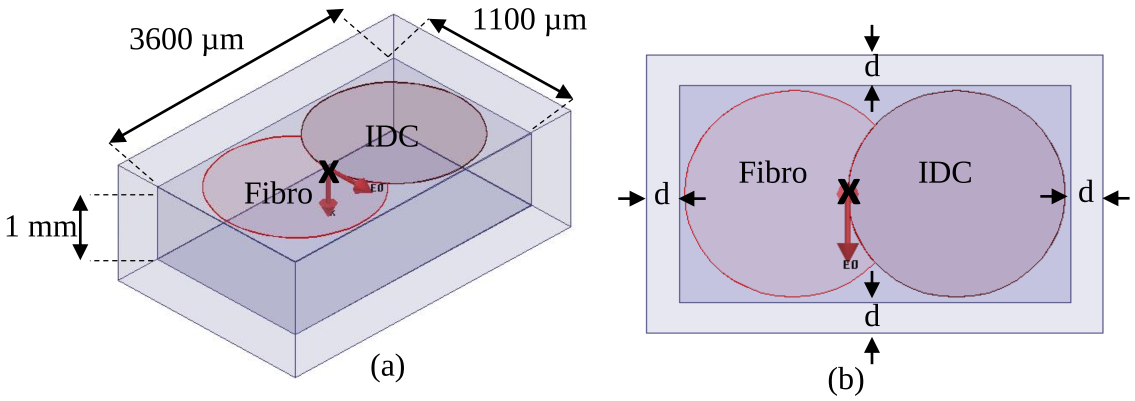

(a)

(b)

Figure 2.9: Reflection imaging convergence model showing location of incident beam.
(a) Isometric view (b) top view.

The convergence data for the 100 µm and 300 µm distance between the PML and the problem domain are presented in Table 2.3 and Table 2.4, respectively.

Table 2.3: Convergence data for 100 µm distance between the PML and the problem domain.

Number of Pass	**Number of Tetrehedra**	**Delta E (dE)**	**Solver Memory (GB)**	**Real Time (hh:mm:ss)**	**CPU time (hh:mm:ss)**	**No of Processors**
1	127948		12.3	0:09:07	0:31:11	16
2	163216	0.084406	19.2	0:19:55	1:24:32	16
3	202094	0.042717	26.1	0:29:15	3:15:41	32
4	257739	0.049365	39.4	0:36:59	5:22:32	32
5	323057	0.035289	56.2	0:37:46	11:52:53	64
6	419182	0.023483	78.1	1:31:22	20:35:24	64
7	456913	0.0054838	85	1:59:06	40:50:05	64
8	572757	0.017204	110	2:44:45	55:43:39	64
9	743507	0.001664	153	4:48:48	85:49:00	64
10	926177	0.012541	200	8:40:00	130:29:16	64
11	1202806	0.011359	269	15:20:30	203:30:55	64
12	1562381	0.0083774	389	31:47:36	322:34:55	64

Table 2.4: Convergence data for 300 µm distance between the PML and the problem domain.

Number of Pass	**Number of Tetrehedra**	**Delta E (dE)**	**Solver Memory (GB)**	**Real Time (hh:mm:ss)**	**CPU time (hh:mm:ss)**	**No of Processors**
1	129894		12.3	0:12:27	1:01:09	16
2	164104	0.11826	20.1	0:26:25	2:49:02	16
3	195917	0.043627	25.5	0:36:23	4:23:30	16
4	242214	0.046108	34.2	0:47:32	6:27:53	16
5	314066	0.037614	50	1:10:33	11:00:52	16
6	396489	0.02393	66.6	1:41:03	17:04:56	16
7	476256	0.013239	83.7	2:18:58	24:59:33	16
8	618241	0.067051	113	2:10:50	46:13:13	32
9	775545	0.014709	150	5:32:59	110:36:59	32
10	1007124	0.013562	214	9:28:28	160:06:50	32
11	1308000	0.012302	275	17:58:05	257:54:08	32
12	1698992	0.0066259	409	25:30:13	228:01:25	32

Table 2.3 and Table 2.4 present the simulation data for the two variations of the distance between the PML and the problem domain. For each adaptive pass, the tables show the total number of tetrahedra that make up the mesh, the error value (dE), the amount of memory used for generating the solution, the real time, and the CPU time. The number of processors used for each adaptive solution, which depends on the availability of computing resource on the Arkansas High Performance Computing Center (AHPCC), is also shown for each adaptive pass.

Fig. 2.10 shows a plot of the dE against the number of adaptive passes for both cases of boundary distance from the problem domain. In both cases, the dE shows a decreasing trend which indicates a converging field solution for the simulation. At the eighth adaptive pass, the case with 300 µm distance between the PML and the problem domain shows a spike in dE value compared to the 100 µm PML distance from problem domain. This may be caused by the large increase observed in the number of tetrahedral elements when the adaptive solution process proceeds from the seventh to the eighth iteration. In the case with 100 µm distance from the model, the percentage increase in the tetrahedral element as the adaptive process moves from the seventh to the eighth iteration was 25.5 %, while it was 29.8 % in case with 300 µm distance from model. This follows logically because the latter has larger computational domain when compared to the former.

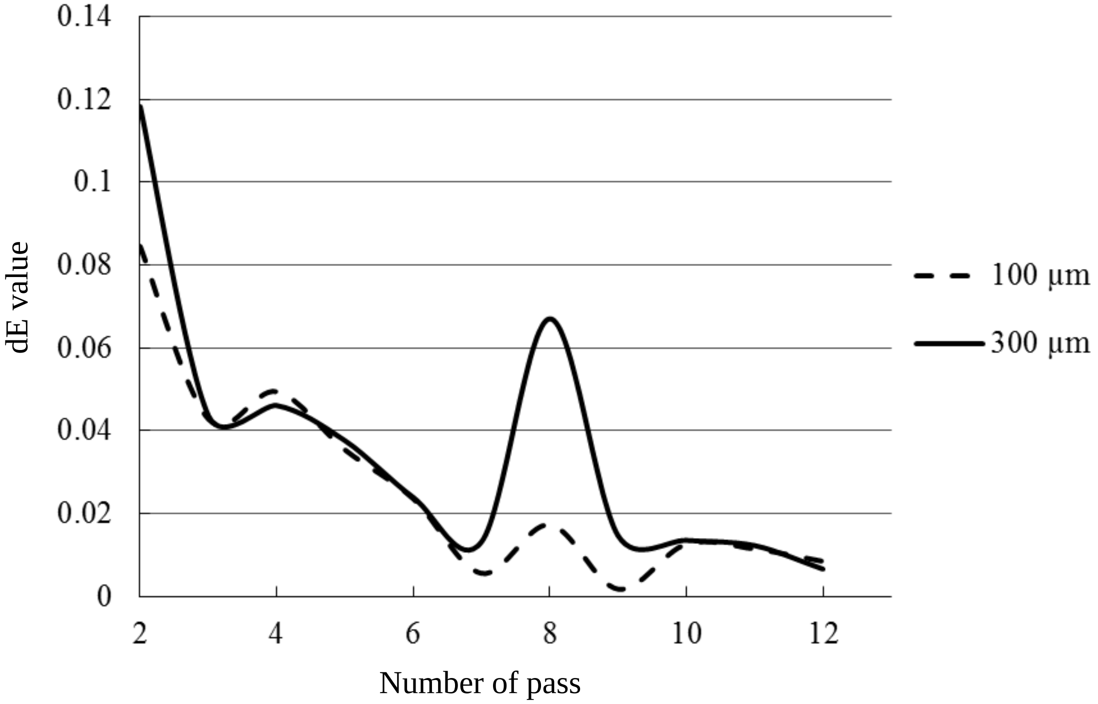

Figure 2.10: The plot of dE versus the number of adaptive pass.

In subsequent simulations, the 300 µm PML distance from the model was used. This was chosen so that images at distances greater than 100 µm from the problem domain can be viewed.

2.4 Alternative Convergence Approach for the HFSS Simulation

Due to the interest in the field solutions in the pixels associated with each incident beam in this simulation, a different approach was employed in setting up the adaptive solution. By default, HFSS provides the field solution for the last iteration of an adaptive solution process. As an example, if an adaptive solution has five adaptive passes or iterations, field solutions can only be viewed and calculated for the fifth adaptive pass. This makes it impossible to track the field convergence at any pixel in the neighborhood of the location of beam excitation.

An alternative approach to track the field solution convergence in the pixels of interest was employed. In this approach, a dependent adaptive solution was used, in which current adaptive iteration was dependent on the solution of the previous one. The present adaptive solution uses the mesh from previous solution and also saves mesh and field data for its solution. This way, each iteration of the adaptive solution had a field solution that could be used to investigate the convergence in the pixel of interest in the simulation.

For a raster location where the Gaussian beam was illuminating the tissue, the average value of the magnitude of the x-component ($|E_x|$) of the electric field was evaluated over the pixel at the top boundary (next to the PML layer). The average of the magnitudes of the x-component of the electric field for a pixel was evaluated as given in Equation 2.1.

$$Average\ |E_x|\ /Pixel = \frac{\oint |E_x|\ dA}{Pixel\ Area} \qquad \text{(Equation 2.1)}$$

Table 2.5 shows the default HFSS dE and the relative error in average $|E_x|$ values between successive passes of the adaptive solution. A plot of these values in Fig. 2.11 shows that the field solution in the pixel converges better and faster than field solutions of the entire model. The values of the average $|E_x|$ in a pixel are an order of magnitude lower than dE for each adaptive pass. Approaching the convergence of simulation in this manner helped reduce the computational resource and time required for this research. From this analysis, the maximum number of adaptive pass for subsequent simulations was set to six as the error in each pixel was of the order of 10^{-3} in the remainder of results of this work.

Table 2.5: HFSS default dE and average |Ex|/ pixel data.

Number of Pass	**HFSS dE**	**Average $\|E_x\|$/Pixel**
2	0.11826	0.000345779
3	0.04363	0.010309334
4	0.04611	0.000309335
5	0.03761	0.00049689
6	0.02393	0.000972209
7	0.01324	0.000714216
8	0.06705	0.000158691
9	0.01471	0.000121262
10	0.01356	0.000117405
11	0.0123	0.000206103

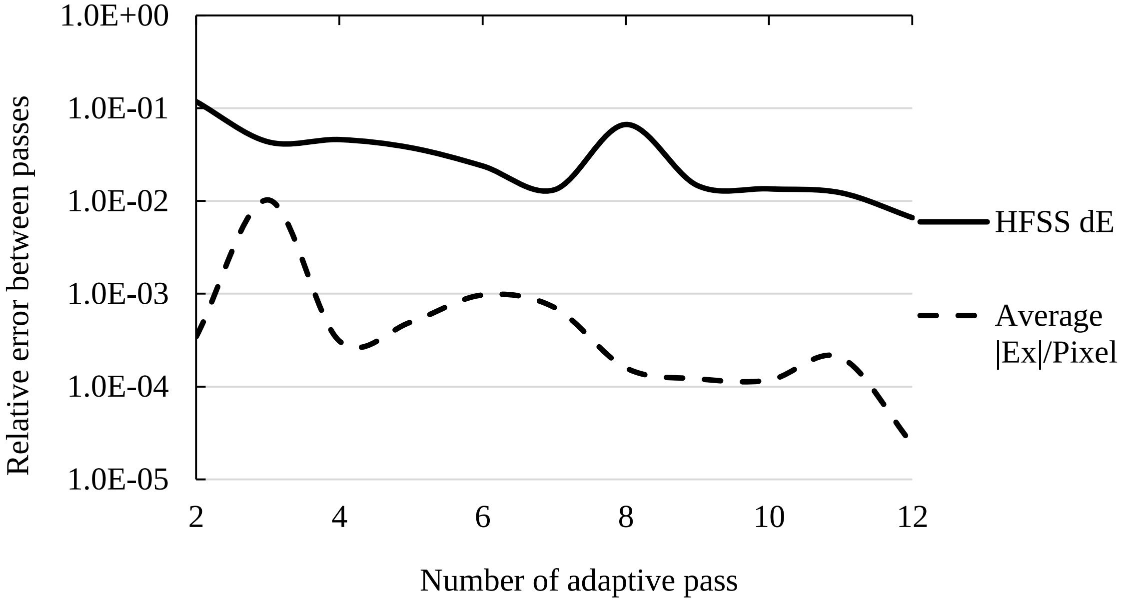

Figure 2.11: Error values versus number of adaptive pass.

2.5 Effect of the Glass Thickness on the Field Solution

In an effort to reduce the simulation time of this problem, an attempt was made to reduce the glass thickness. The glass thickness was of interest because it contained the largest amount of finite element tetrahedral meshes and, consequently, increased the computational time and cost of the problem. Fig. 2.12 shows the y-z cross-section of mesh elements after the fourth adaptive pass.

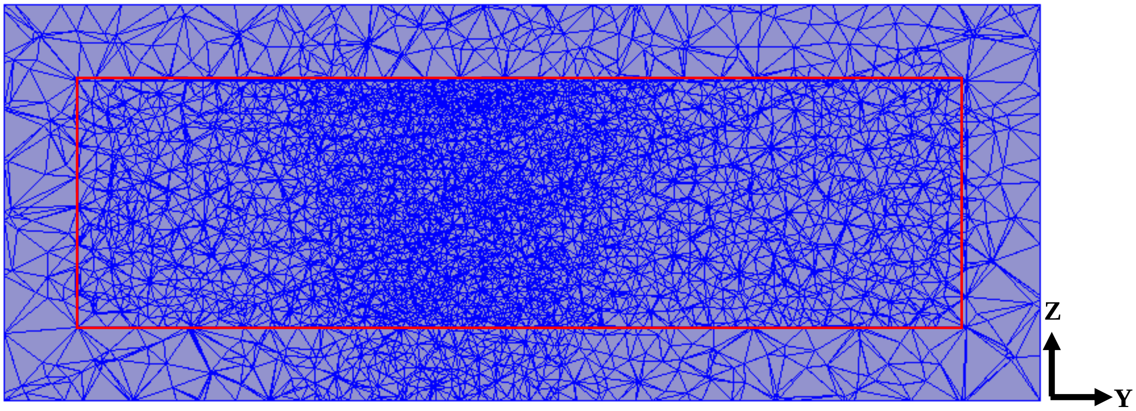

Figure 2.12: Mesh element in computational domain showing the glass cross-section in red rectangle.

The red color rectangle in Fig. 2.12 shows the cross section of the glass in the computational domain. The glass part of the simulation model has the highest concentration of the tetrahedral mesh elements. A large number of tetrahedral mesh elements increases the simulation time and the cost, as shown in Table 2.3 and Table 2.4 of section 2.3. Fig. 2.13 shows the percentage distribution of the tetrahedral elements in each region of the model. In all iterations, the number of elements in glass accounts for more than 80 % of the total mesh elements in the entire model. Therefore, reducing the size of the glass would significantly reduce the computational time and cost for solving for the fields.

In order to determine the glass thickness to use so the simulation time could be reduced, the total E-field as THz beam propagates in the glass was investigated. Fig. 2.14 shows a y-z cross section through the beam axis of the magnitude of total electric field (E-field) in the computational domain.

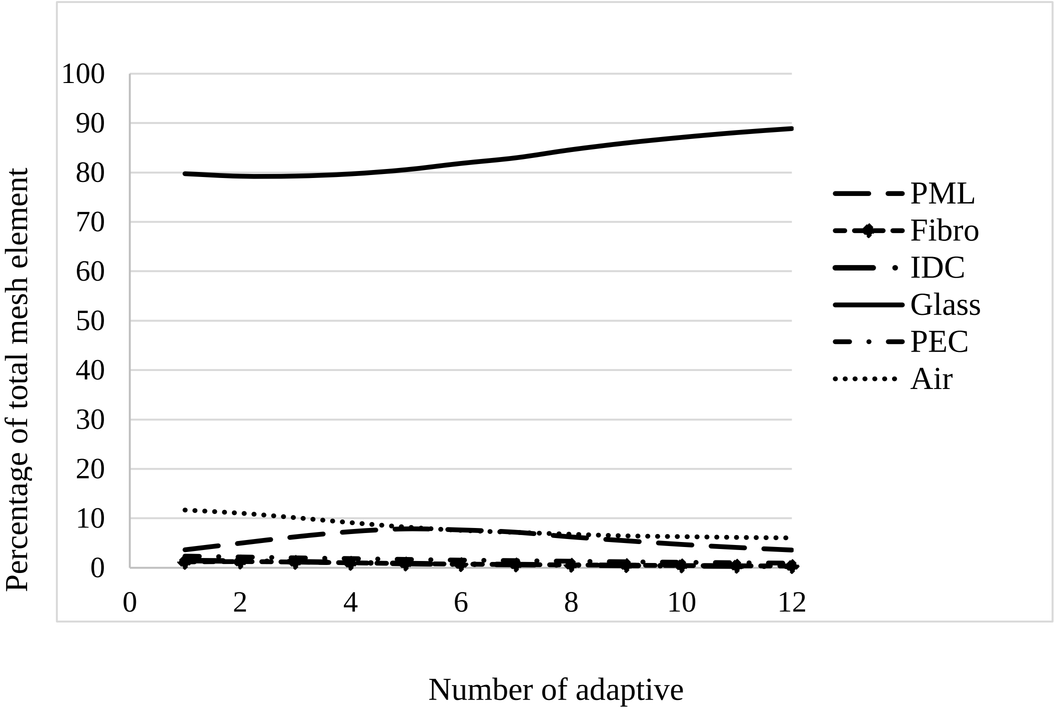

Figure 2.13: Percentage of mesh elements in computational domain at different adaptive pass.

The total E-field was attenuated significantly as it propagated in the glass as shown in Fig. 2.14. To see the attenuating effect of the glass clearly, the magnitude of the total E-field was plotted along a line that passes through the axis of the Gaussian beam, and extends through the entire domain. The line along which the total E-field was plotted is shown as the green line in Fig. 2.14.

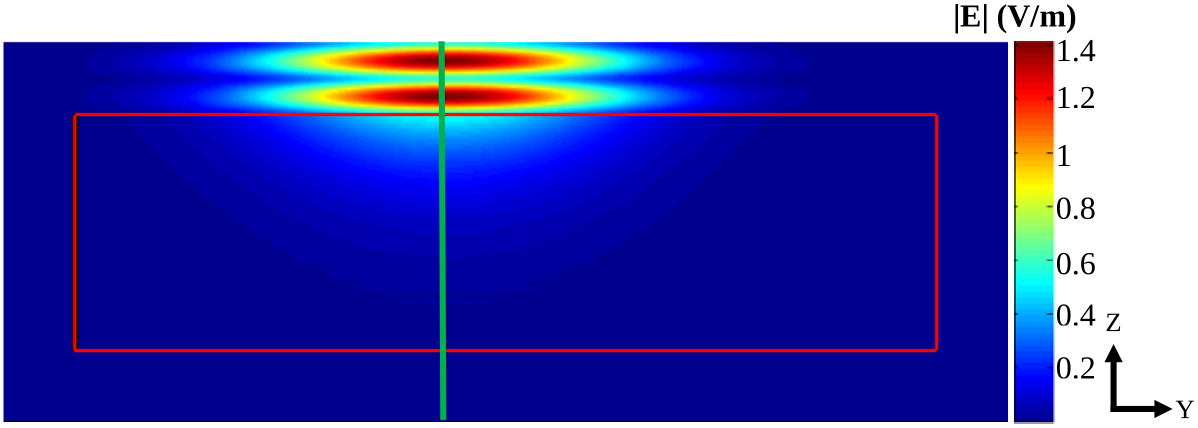

Figure 2.14: Y-Z cross section of magnitude of total E-field.

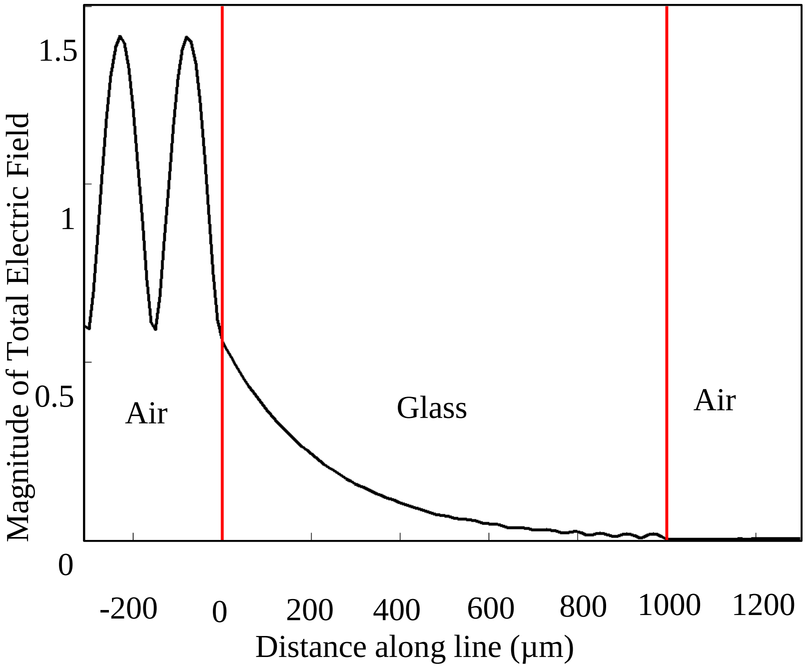

Figure 2.15: Magnitude of total E-field along a line through Gaussian beam axis.

Fig. 2.15 shows the plot of the magnitude of the total E-field along the green line of Fig. 2.14. The region of glass is shown to start at 0 µm, above which there was the thin tissue region (not shown in Fig. 2.15). At the beginning of the glass region, the total E-field magnitude was

0.5581 V/m, and 600 µm into the region, the total E-field magnitude had been attenuated to 0.04468 V/m. This implied that at 600 µm into the glass, 92 % of the E-field magnitude at the top of the glass had been attenuated. Therefore, a glass thickness of 600 µm was investigated in the simulation. For the 600 µm glass thickness to be considered a good approximation to the 1 mm glass thickness, it was expected that there would be no significant difference in field solutions between the two variations. Fig. 2.16 shows the magnitude of scattered E-field after 12 adaptive iterations at the top boundary for the two variations of glass thicknesses. Fig. 2.16 shows a significant difference in the field solution between both variations.

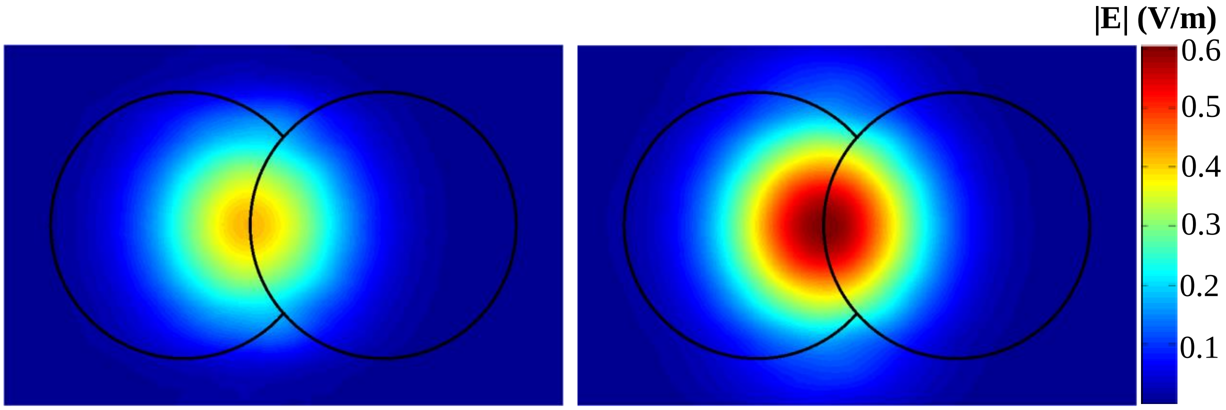

(a) (b)

Figure 2.16: Scattered E-field at top boundary showing tissue outline (a) 1mm thick glass (b) 600 µm thick glass.

The magnitude of the scattered E-field shown in Fig. 2.16a for the case with 1 mm glass thickness was lower when compared to the case of 600 µm glass thickness (see Fig. 2.16b). Thus, the field solutions obtained by reducing the glass thickness to 600 µm did not give a good approximation when compared to those from the actual glass thickness used in the experiment. The actual glass thickness of 1 mm used for the experimental measurements was, therefore, retained in all subsequent reflection imaging simulations investigated in this work.

2.6 Effect of Tissue Model Thickness on Field Solution

An important observation from the magnitude of the scattered E-field of Fig. 2.16 was that the field values reflected from the two regions of the tissue model: Fibro and IDC, were almost the same. It was expected that different parts of the tissue model would reflect different E-field values because of their different material properties given in Table 2.1. However, as shown Fig. 2.16a, and Fig. 2.16b, there was no significant difference in the field reflected from the Fibro and IDC regions of the tissue even with the Gaussian beam excitation extending into both regions. This led to an investigation of the reflected E-field from both regions of the tissue model independently.

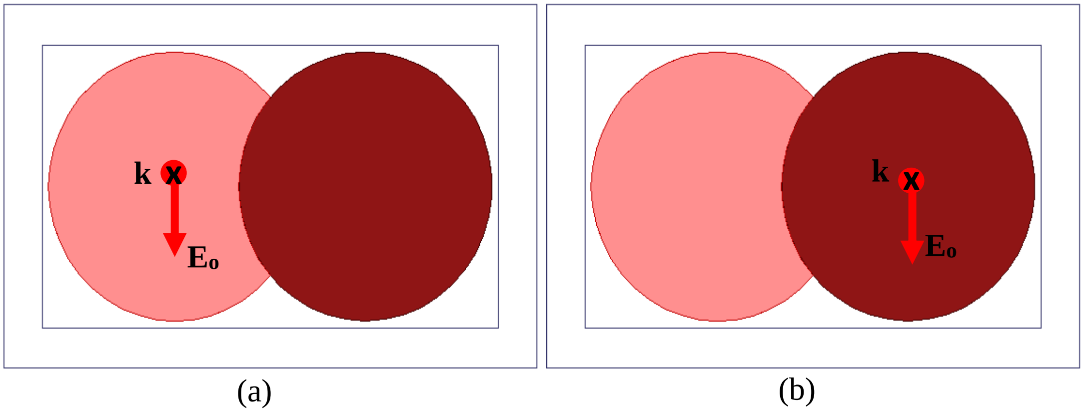

(a) (b)

Figure 2.17: Gaussian beam location for the 10 µm thick tissue (a) At the center of fibro region (b) at the center of IDC region.

The Gaussian beam excitation was placed at the center of each tissue regions as shown Fig. 2.17. Fig. 2.17a and Fig. 2.17b show beam at the center of Fibro and IDC regions of the tissue respectively. The magnitude of the scattered E-field at the top boundary for both regions was plotted together as shown in Fig. 2.18.

Fig. 2.18 confirmed observation made from Fig. 2.16. The different regions of the tissue could not be differentiated with the 10 µm thick tissue model. This trend of not being able to differentiate parts of breast cancer tissue was also a challenge in the experimental measurements using THz imaging system. A new model with 40 μm thick tissue was investigated here. The magnitude of the scattered E-field from the different regions of the 40 μm thick tissue model is shown in Fig. 2.19.

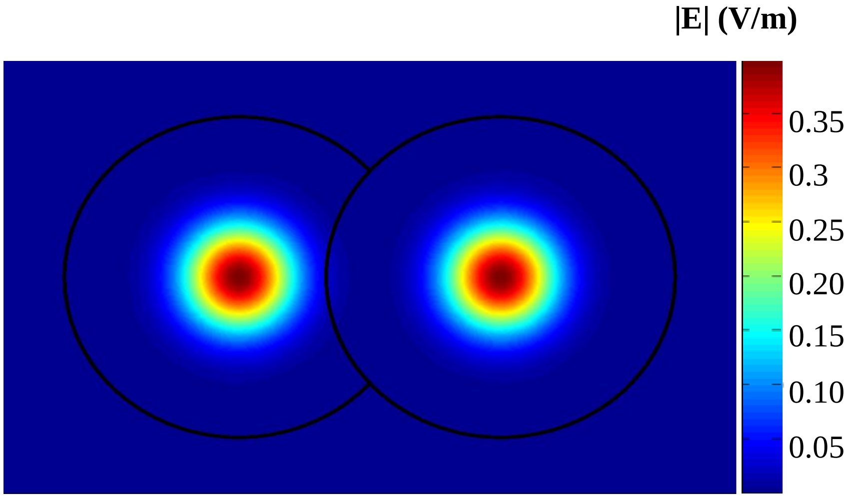

Fig. 2.18: Scattered E-field from centers of the 10 μm tissue.

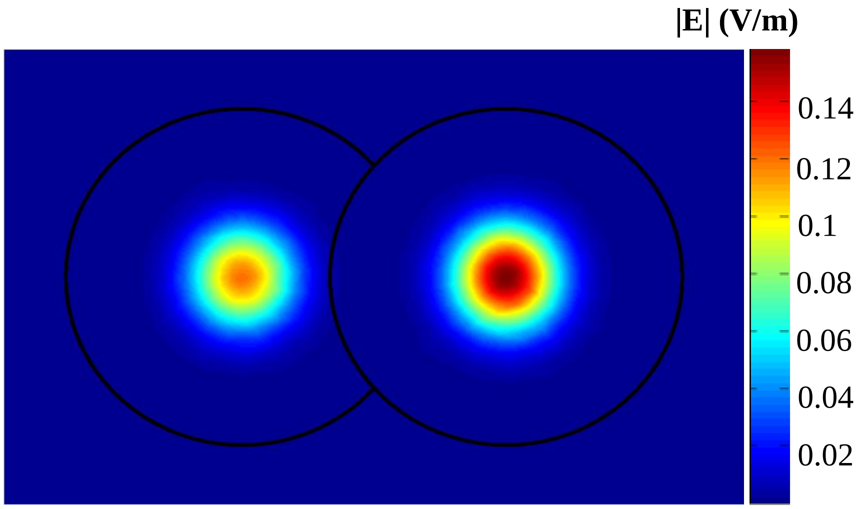

Figure 2.19: Scattered E-field from centers of the 40 μm tissue.

The 40 µm tissue model showed a clear differentiation of the regions as shown in Fig. 2.19. Those results agree with experimental measurements that thicker tissue sections were found to provide better differentiation of tissue types. All further simulations in this research were thus carried out using the 40 µm thick tissue models.

3. Results and Discussion

This chapter presents simulated THz images of several models considered in this work. First, images of the reflection mode convergence model described in section 2.3.1 (see Fig. 2.3 of section 2.3.1) is presented. Then, irregular HFSS tissue models that mimic actual breast cancer tissue samples are presented. These cancer tissue samples used for creating the models were the ones used in the experimental work reported by Bowman [13].

3.1 HFSS Convergence of Simulated THz Images of Reflection Mode

The image of the convergence model shown in Fig. 3.1, was first created by scanning the incident Gaussian beam in 200 µm steps across the tissue model. The step size of 200 µm created a grid of points which were located at the center of a 200 µm x 200 µm square pixels. Due to the symmetry of the convergence model, half of the model was simulated. The line of symmetry of the model and the area over which the Gaussian beam was scanned are shown by the red dashed line and dashed rectangle, respectively, in Fig. 3.1b. The scanned area (dashed rectangle in Fig. 3.1b) had a dimension of 3600 µm x 1100 µm and contained 114 raster points where the Gaussian beam was incident (see Fig. 3.2).

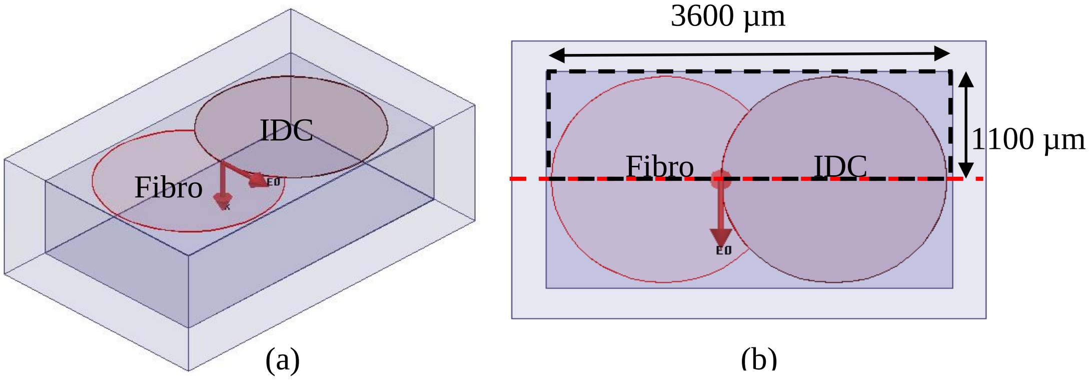

Figure 3.1: Convergence model for reflection imaging mode. (a) Isometric view (b) top view showing symmetry line and dimension of area imaged.

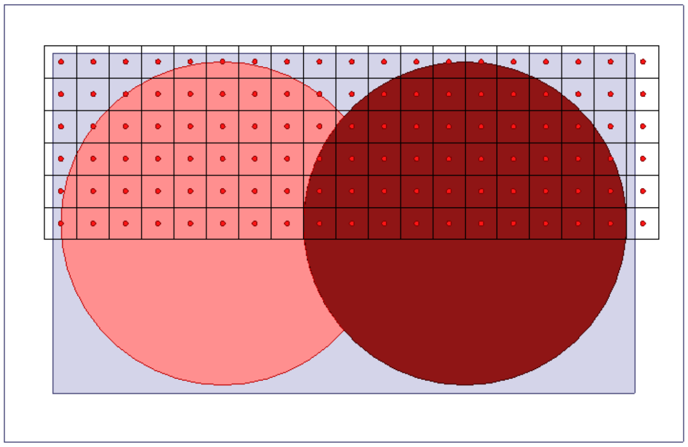

Figure 3.2: Top view of convergence model showing the raster point in red dots that the Gaussian beam is scanned over the model.

A parametric setup of the raster locations of the beam was done in HFSS to scan the beam over the tissue model. Table 3.1 provides more simulation data for this model including the dimension of glass slide on which the tissue was imaged, the memory required to solve for field when beam is incident at a raster point, the total memory requirement for storing the results, and the total time of the simulation. The solver memory, which is the peak amount of random access memory (RAM) for the simulation [30], given in the Table 3.1 is the solver memory for the first raster location. Solver memories for other raster points vary within 10 % of this value.

Table 3.1: Simulation data of convergence model scanning beam in 200 µm steps.

Simulation Data	**Value**
Dimension of glass slide in simulation	2100 µm x 3600 µm x 1 mm
Dimension of area imaged	1100 µm x 3600 µm
# of raster points in imaged area	114
Solver memory for first raster point (GB)	43.5
Storage memory for field solution (GB)	34
Total real time for Simulation (hh:mm:ss)	90:50:58

The images were created by averaging the magnitude of the scattered electric field (E-field) for each pixel as shown in Fig. 3.3. As an example, in Fig. 3.3, the first raster location numbered 1 had the Gaussian beam axis on the red spot, and the average of field values were computed over the blue square pixel using Equation 2.1. The process was repeated for all the raster locations. The field was first evaluated over each pixel at the top boundary above the tissue. The values of the E-field over other constant z planes are presented in a later section of this chapter. A 2D matrix of field values corresponding to each raster location was plotted in MATLAB.

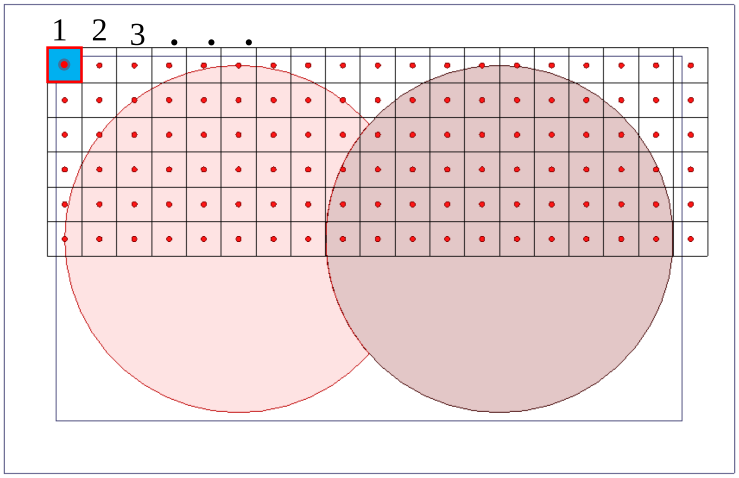

Figure 3.3: Convergence model showing the pixel (color blue) over which average field values was evaluated for the raster position 1.

The image created for the convergence model by scanning the Gaussian beam in 200 µm steps over the model is shown Fig. 3.4 and Fig. 3.5. Fig. 3.4 shows the image of the convergence model viewed at the top boundary of the domain next to the PML layer. An outline of the tissue is also shown in the image by the black line. All subsequent images have the outline of the tissue shape projected on any plane where images were observed. The reflected field from the glass region of the model was much higher than other regions (Fibro and IDC), making it difficult to clearly differentiate between the fibro and IDC regions of the HFSS tissue model (see Fig. 3.4). In order to differentiate the other regions of the model which are the regions of interest in this thesis, the color bar of the image was adjusted accordingly (see Fig. 3.5). Subsequent images for other tissue models simulated in this work are presented with the adjusted color bar scale to show the different regions of the HFSS tissue models.

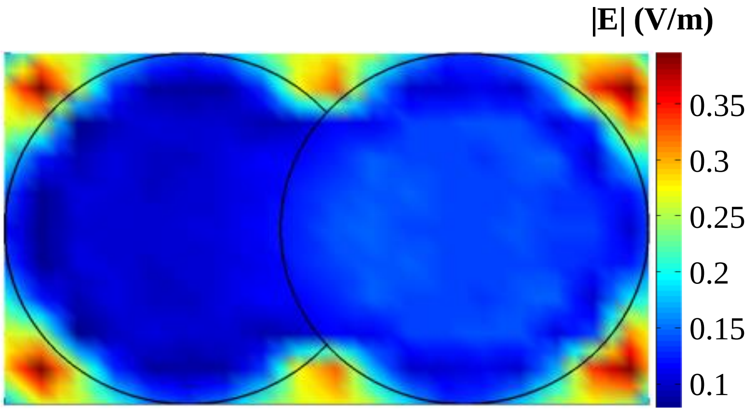

Figure 3.4: Simulated image of convergence model using 200 µm x 200 pixels µm at the top boundary of domain.

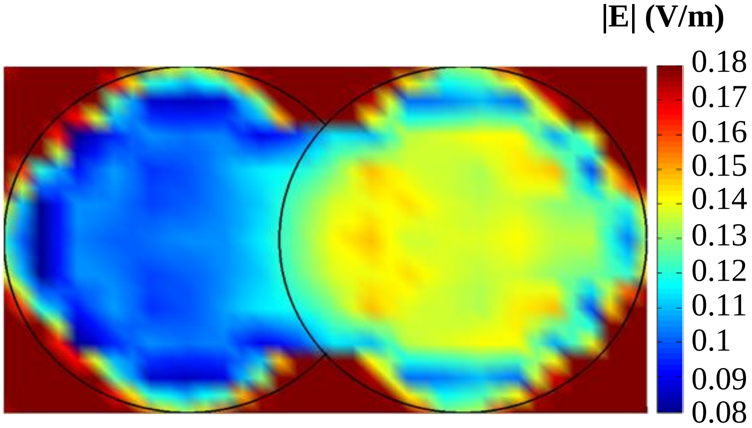

Figure 3.5: Simulated image of convergence model using 200 µm x 200 µm pixels at the top boundary of domain with adjusted color.

The E-field reflected from the IDC region is higher than that from the Fibro region as expected and a clear differentiation of the fibro and IDC could be seen. However, the image quality of the convergence model shown in Fig. 3.4 and Fig. 3.5 was not very good because of the large pixel size (200 µm x 200 µm) used in creating the image. In order to improve the image quality, the step size for scanning the Gaussian beam in the simulation was reduced from 200 µm to 100 µm. The new image of the model was created by averaging the field over 100 µm x 100 µm pixel.

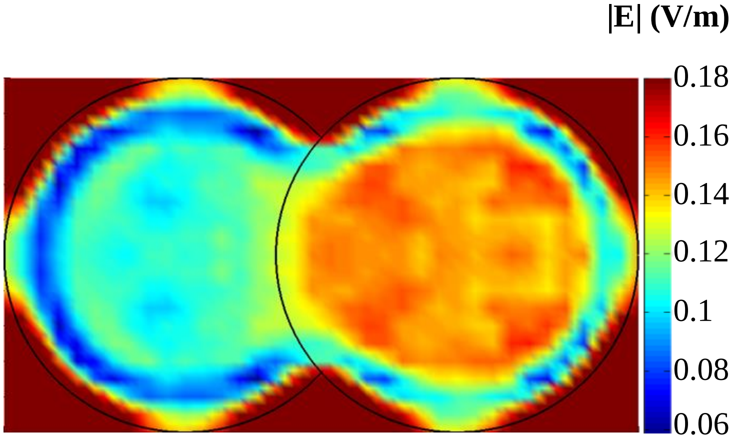

Figure 3.6: Simulated image of convergence model using 100 µm x 100 µm pixels at the top boundary of domain.

The image created using the 100 µm x 100 µm pixel (see Fig. 3.6) showed the two regions of the tissue clearer than that created using the 200 µm x 200 µm pixel. However, the better image was obtained at a higher computational cost (see Table 3.2). The data in this table shows that the new simulation time increased by 280%. The images from the two pixel size variations are shown in Fig. 3.7 for comparison. Subsequent tissue models were thus simulated by scanning the Gaussian beam in 100 µm steps over the tissue model, creating 100 µm x 100 square pixels.

Table 3.2: Simulation data of convergence model scanning beam in 100 µm steps.

Simulation Data	**Value**
Dimension of glass slide in simulation	2100 µm x 3600 µm x 1 mm
Dimension of area imaged	1100 µm x 3600 µm
# of raster points in imaged area	396
Solver memory for first raster point (GB)	47.3
Storage memory for field solution (GB)	119
Total real time for simulation (hh:mm:ss)	254:58:33

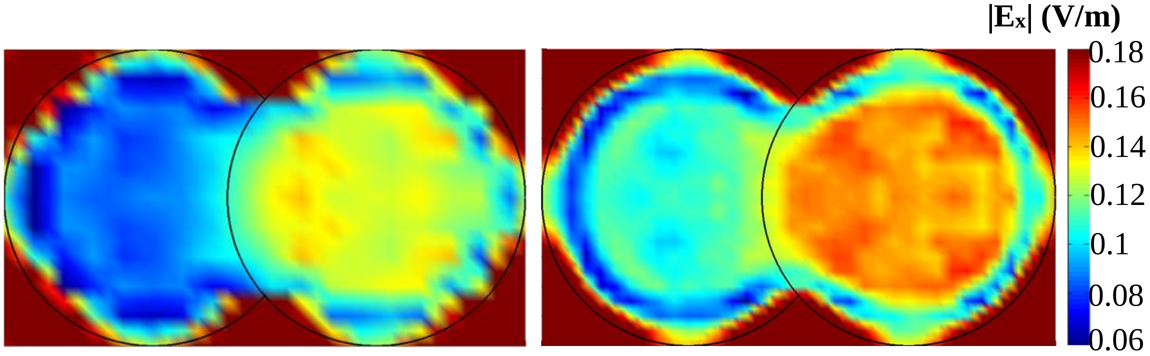

Figure 3.7: Convergence model simulated reflection mode images. (a) Using 200 µm x 200 µm pixels, (b) using 100 µm x 100 µm pixels.

3.2 HFSS Simulated Images of the Reflection Mode of Realistic Tissue samples

Tissue models that mimic the realistic breast cancer tissue samples used in the experimental measurements conducted by others in the group [2], [13], [14], were simulated using HFSS. The cancer tissue samples used in the experimental work were obtained from the National Disease Research Interchange (NDRI) [13], [14]. The pathology assessment of the breast cancer tissue samples differentiating between Infiltrating Ductal Carcinoma (IDC)–the cancer tissue, and fibro glandular (Fibro)–the healthy tissue, was conducted by the Northwest Arkansas Pathology Associates P.A. [14]. The pathology images were used for creating the

HFSS tissue models that were simulated in this research. Four different tissue models were simulated and the reflection mode images are presented in this section.

3.2.1 HFSS Tissue Model #1

The cancer tissue sample used to create the first HFSS model was obtain from a 54-year old black woman diagnosed with IDC [13]. The pathology image of the cancer tissue sample used to create this model is shown in Fig. 3.8. The IDC and fibro regions of the tissue are clearly indicated in the figure.

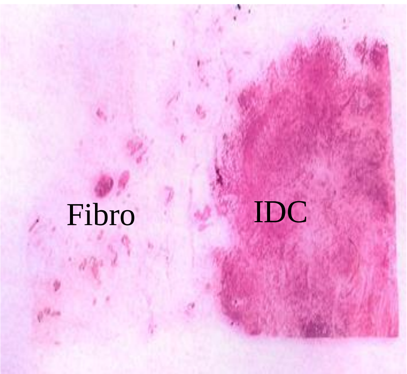

Figure 3.8: Low power pathology image for HFSS tissue model #1[13].

The isometric and top views of the HFSS model created from the pathology image of Fig. 3.8 are shown in Fig. 3.9a and Fig. 3.9b, respectively.

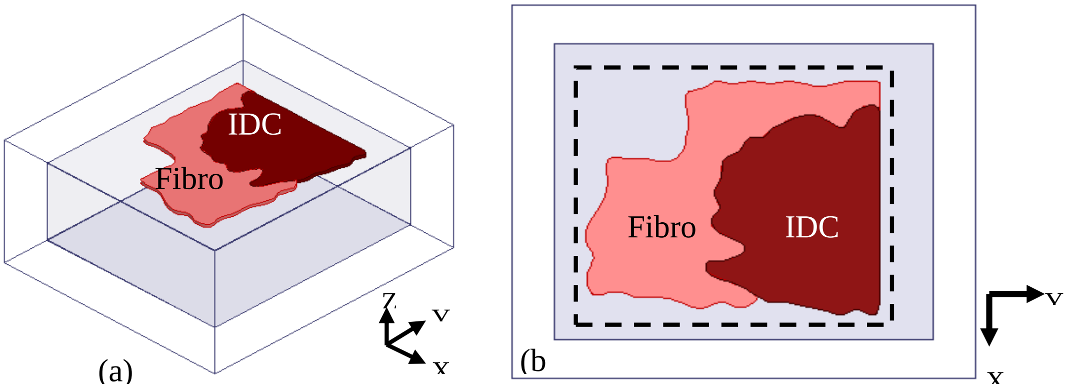

Figure 3.9: HFSS Tissue Model #1. (a) Isometric view (b) top view showing imaged area in dashed rectangle.

The imaged area shown by the dashed rectangle in Fig 3.9b contained 483 raster scan locations when the incident Gaussian beam was scanned over the area in 100 µm steps. Other simulation data for this model are presented in Table 3.3.

Table 3.3: Simulation data of HFSS tissue model #1.

Simulation Data	**Value**
Dimension of glass slide in simulation	2300 µm x 2700 µm x 1 mm
Dimension of area imaged	2100 µm x 2300 µm
# of raster points in imaged area	483
Solver memory for first raster point (GB)	34
Storage memory for field solution (GB)	114
Total real time for simulation (hh:mm:ss)	286:36:47

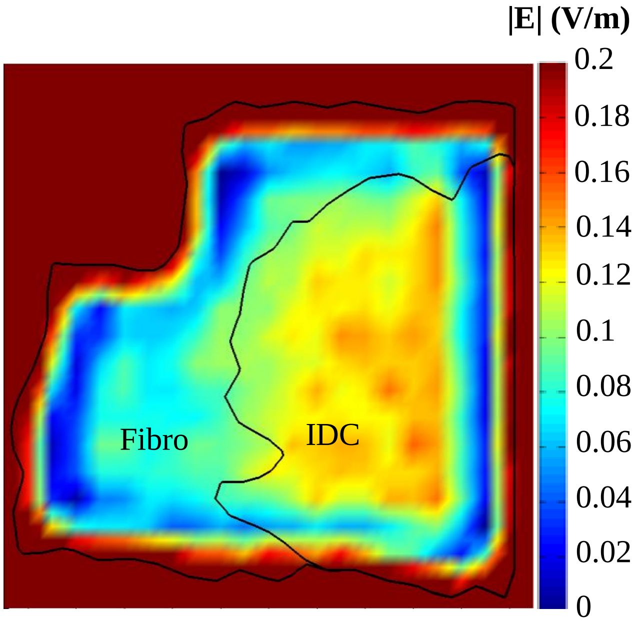

Figure 3.10: HFSS tissue model #1 reflection mode simulated image created by raster scanning the Gaussian beam in 100 µm step size, and averaging E-field over 100 µm x100 µm pixel.

The simulated reflection image of Fig. 3.10 shows a clear differentiation among the IDC, Fibro, and glass regions of the HFSS tissue model. The black outline in the figure represents the projection of the tissue shape on the surface at which the image was created (at the top boundary of the problem domain in this case). The reflected field from the glass region is the highest of all reflected fields from the regions of the model. This was due to the high relative permittivity and conductivity of glass at 1 THz and other regions of the problem domain reflected field accordingly based on their electrical properties. Also, there was higher reflection from the IDC region when compared to reflection from the fibro region.

Before simulating other tissue models, an enhancement of the image was thoroughly investigated using the HFSS tissue model #1. Just as it was in the case of the convergence model of section 3.1, it was expected that reducing the step size for scanning the Gaussian beam over the tissue model would improve the quality of the simulated images. However, this reduction would come at a cost of increased simulation time and computational resources similar to the case of the convergence model discussed earlier in section 3.1. In order to improve the image without necessarily increasing the computational cost, the magnitude of the E-field was averaged over smaller areas of 50 µm x 50 µm without changing the step size for scanning the Gaussian beam to 50 µm. In other words the Gaussian bean scan size was kept at 100 µm. This kept the computational cost and time the same. However, post-processing involving averaging of E-field magnitude was obtained over a smaller 50 µm x 50 µm pixel area and not over 100 µm x 100 µm pixel as was the case for the image of Fig. 3.10. Averaging the magnitude of the E-field over 50 µm x 50 µm pixel improved the image when compared to averaging over 100 µm x 100 µm pixel (see Fig. 3.11). Thus, averaging the field over a 50 µm x 50 µm pixel and scanning the Gaussian beam in 100 µm step size were used for creating images of subsequent models.

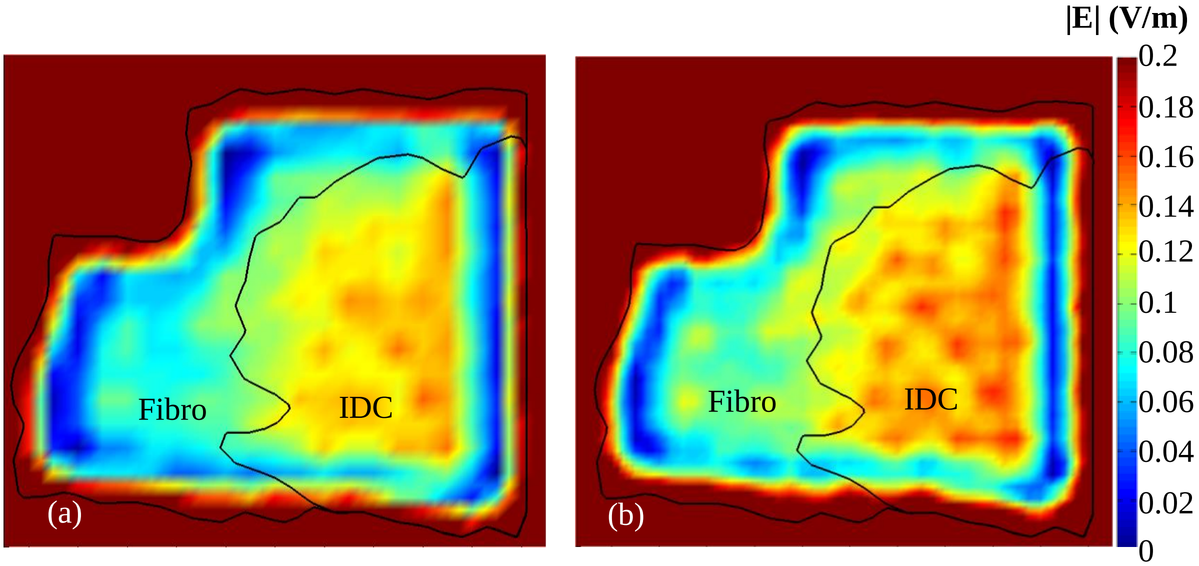

Figure 3.11: HFSS tissue model #1 reflection mode image. (a) 100 µm Gaussian beam step size with field averaged over 100 µm x 100 µm pixel, (b) 100 µm Gaussian beam step size with field averaged over 50 µm x 50 µm pixel.

3.2.2 HFSS Tissue Model #2

The cancer tissue sample used for creating this HFSS model was obtained from a 46-year old Caucasian woman, and the pathology image is shown in Fig. 3.12. Isometric and a top views of the HFSS model created for the tissue sample are shown in Fig. 3.13.

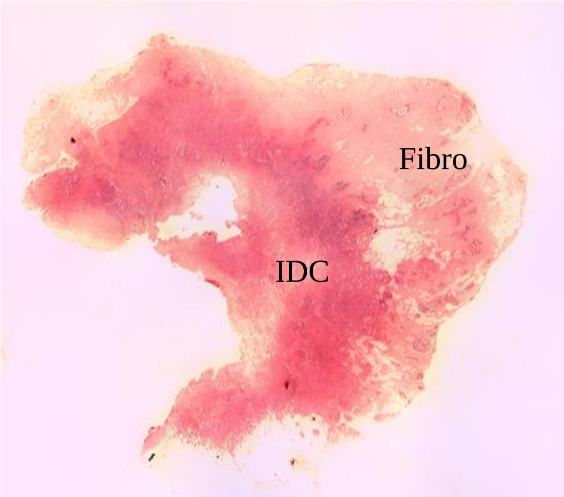

Figure 3.12: Low power pathology image for HFSS tissue model #2 [13].

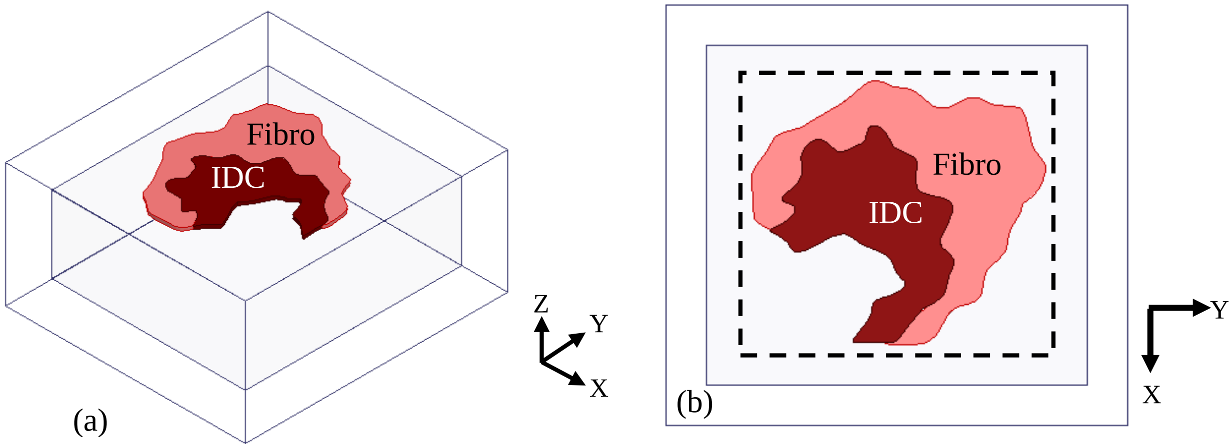

Figure 3.13: HFSS tissue model #2. (a) Isometric view (b) top view showing imaged area in dashed rectangle.

The imaged area shown by the dashed rectangle in Fig. 3.13b contained 506 rectangular grid points where the Gaussian beam was incident. Table 3.4 provides simulation information about this tissue model.

Table 3.4: Simulation data of HFSS tissue model #2.

Simulation Data	**Value**
Dimension of glass slide in simulation	2500 µm x 2800 µm x 1 mm
Dimension of area imaged	2200 µm x 2300 µm
# of raster points in imaged area	506
Solver memory for first raster point (GB)	45
Storage memory for field solution (GB)	162
Total real time for simulation (hh:mm:ss)	361:41:40

The image created for HFSS Tissue model showing an outline of the tissue shape is shown in Fig. 3.14. The image shows a clear differentiation of all the regions of the tissue, with the glass region having the highest reflection of the E-field of all the regions. The reflected E-field from the IDC region is higher than the reflected field from the Fibro region. A fourth region, also observed in the image of HFSS tissue model#1(see Fig. 3.10 and Fig. 3.11), can also be seen here, even though there is no fourth region in the simulated models. This region appears as an artifact of a low field region that surrounds the tissue region of the model. Further investigation into this artifact low field region surrounding the tissue is reported in Section 3.3 of this chapter.

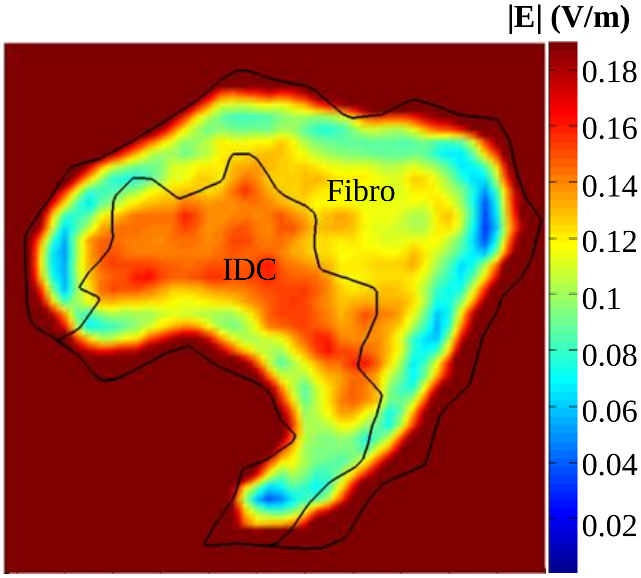

Figure 3.14: HFSS tissue model #2 reflection mode simulated image. E-field averaged over 50 µm x 50 µm pixel, and Gaussian beam scanned in 100 µm steps.

3.2.3 HFSS Tissue Model #3

This HFSS model was created using a cancer tissue sample obtained from a 39-year old Caucasian woman. The pathology image of the breast cancer tissue sample is shown in Fig. 3.15. The isometric and top views of the HFSS model created for the tissue sample are shown in Fig. 3.16a and Fig. 3.16b, respectively.

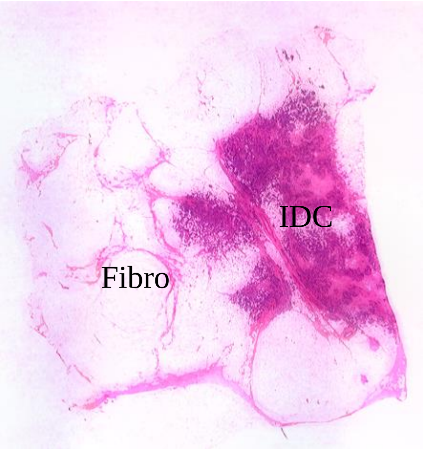

Figure 3.15: Low power pathology image for HFSS tissue model #3 [13].

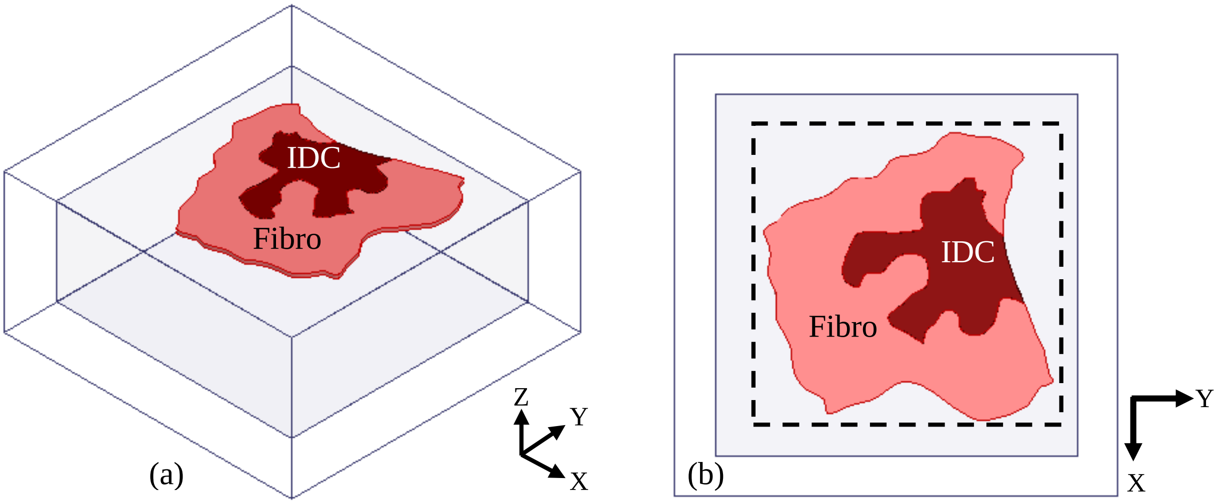

Figure 3.16: HFSS Tissue Model #3 (a) isometric view (b) top view showing imaged area in dashed rectangle.

The area imaged contained 576 raster points. Other simulation data are shown in Table 3.5. The simulated image for this tissue model is shown in Fig. 3.17. The simulated model shows a similar image trend as seen in model #1 and model #2. The highest reflected field observed from the glass side, and a higher reflected field from the IDC when compared to the fibro region.

The artifact of low field region was also present for this tissue model similar to other simulated models.

Table 3.5: Simulation data of HFSS tissue model #3.

Simulation Data	**Value**
Dimension of glass slide in simulation	2700 µm x 2700 µm x 1 mm
Dimension of area imaged	2400 µm x 2400 µm
# of raster points in imaged area	576
Solver memory for first raster point (GB)	44
Storage memory for field solution (GB)	163
Total real time for simulation (hh:mm:ss)	639:08:21

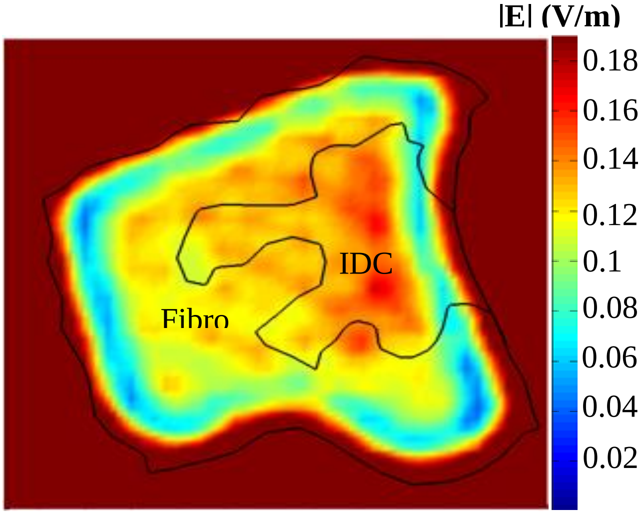

Figure 3.17: HFSS tissue model #2 reflection mode image. E-field averaged over 50 µm x 50 µm pixel, and Gaussian beam scanned in 100 µm steps.

3.2.4 HFSS Tissue Model #4

This model was created based on a breast cancer tissue sample from a 22-year old Caucasian woman diagnosed with IDC [13]. The pathology image and the simulated tissue model in HFSS are shown in Fig. 3.18 and Fig. 3.19, respectively. The simulation data and the simulation image are also shown in Table 3.6 and Fig. 3.20, respectively.

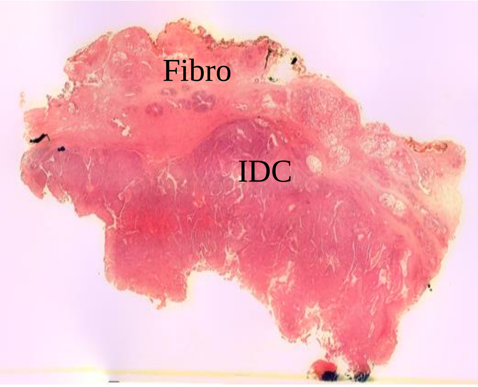

Figure 3.18: Low power pathology image for HFSS tissue model #4 [13].

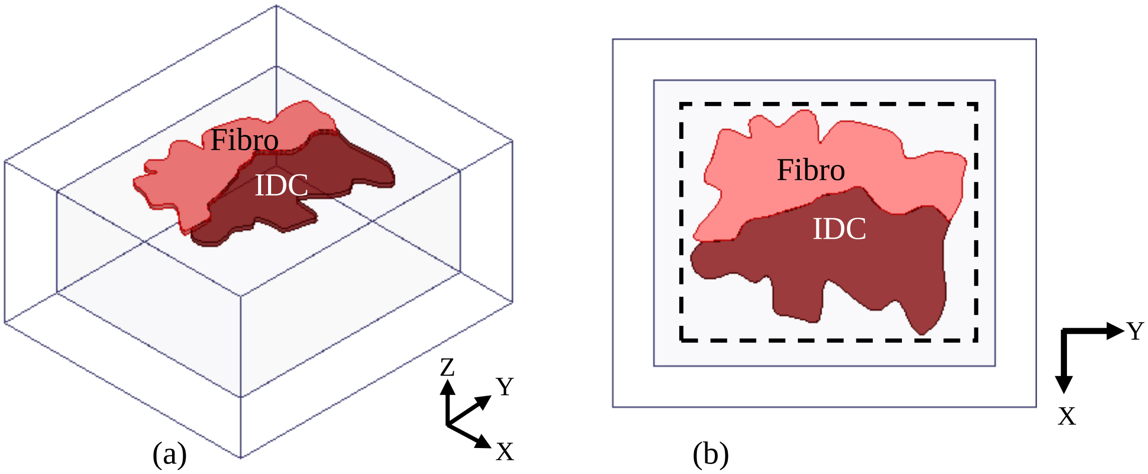

Figure 3.19: HFSS tissue model #4. (a) Isometric view (b) top view showing imaged area in dashed rectangle.

The imaged area shown by the dashed rectangle in Fig. 3.19b contained 396 rectangular grid points where the Gaussian beam was incident. Table 3.6 provides simulation data about the tissue model. The image shows a similar trend to the images obtained for other tissue models. Also, the artifact of low field region surrounding the tissue appeared in all tissue models. This region is investigated in the following section.

Table 3.6: Simulation data of HFSS tissue model #4.

Simulation Data	**Value**
Dimension of glass slide in simulation	2500 µm x 2800 µm x 1 mm
Dimension of area imaged	2200 µm x 2300 µm
# of raster points in imaged area	396
Solver memory for first raster point (GB)	50.5
Storage memory for field solution (GB)	126
Total real time for simulation (hh:mm:ss)	191:50:21

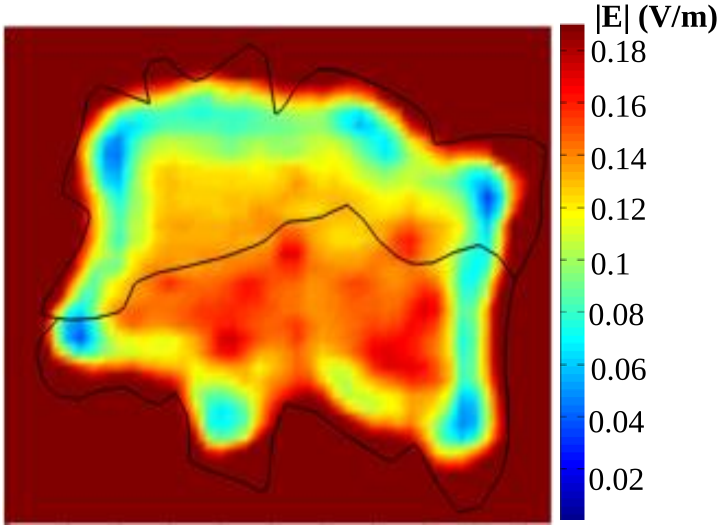

Figure 3.20: HFSS Tissue Model #2 reflection mode simulated image. E-field averaged over 50 µm x 50 µm pixel, and Gaussian beam scanned in 100 µm steps.

3.3 Effect of Mesh Refinement on HFSS Simulated Images

A common trend in all the images created using HFSS tissue models was the region of low E-field magnitudes that surrounded the tissue regions of the models. This border shows up as light blue or blue color around the tissue regions, making the images of the tissue regions for all the models appear smaller than their actual sizes. This artifact border was observed in all four

HFSS tissue model images presented so far in this section (for convenience see Fig. 3.21). In all these images, the field was calculated at the top boundary of the domain as shown in Fig. 3.22.

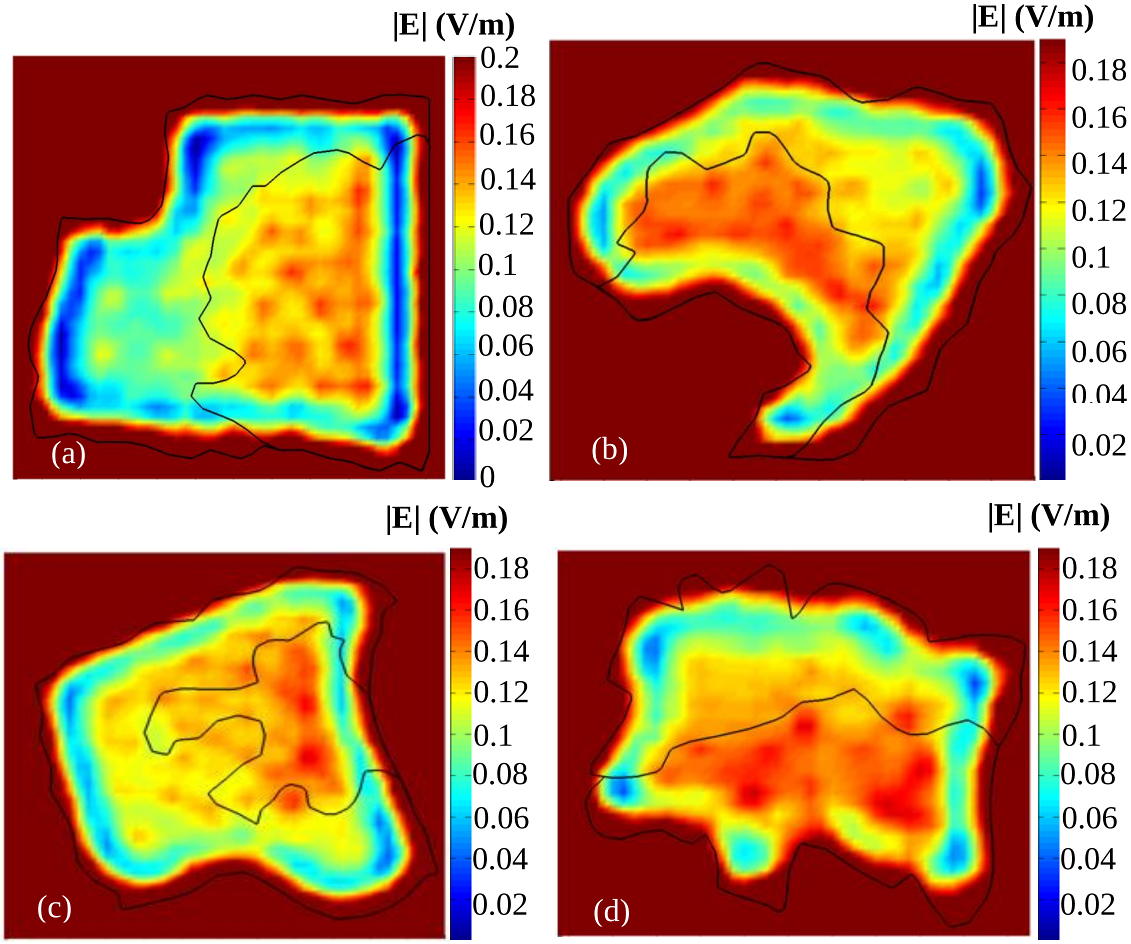

Figure 3.21: HFSS simulated images showing low e-field border around tissue region (a) HFSS tissue model #1 (b) HFSS tissue model #2 (c) HFSS tissue model #3 (d) HFSS tissue model #4.

The cause of the low field border surrounding the tissue region of the HFSS models was investigated by looking at how refined the tetrahedral mesh was at the top boundary where the image was created. Using HFSS tissue model #4, the y-z cross section of the mesh along the first raster location of the Gaussian beam was investigated as shown in Fig. 3.22. The mesh is well refined on the left side of Fig. 3.22 because the axis of the incident Gaussian beam is around that part of the computational model, and HFSS refines the mesh more around areas with excitation in order to get accurate field solutions.

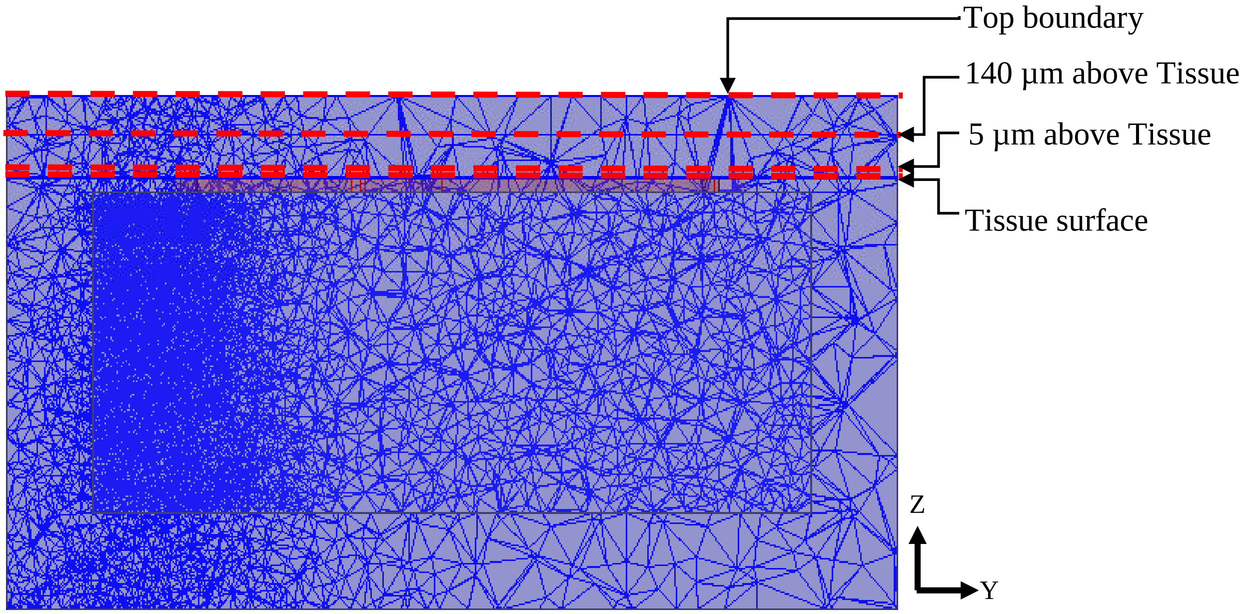

Figure 3.22: y-z Cross section of mesh for HFSS tissue model #1 through first raster location.

The mesh at four different planes were investigated: the top boundary of the domain, the top of tissue, 5 µm above the tissue and, 140 µm above the tissue as shown by the red dashed lines of Fig. 3.22. The x-y cross section of meshes for these planes are shown in Fig 3.23. The mesh at the top boundary (see Fig. 3.23a) is not as refined as the other cross sections shown in Fig. 3.23. The mesh got finer closer to the surface of the tissue model and got coarser further away from it. The raster scan location of the Gaussian beam is shown as the red dot in the Fig. 3.23. The images from the different planes are shown in Fig. 3.24.

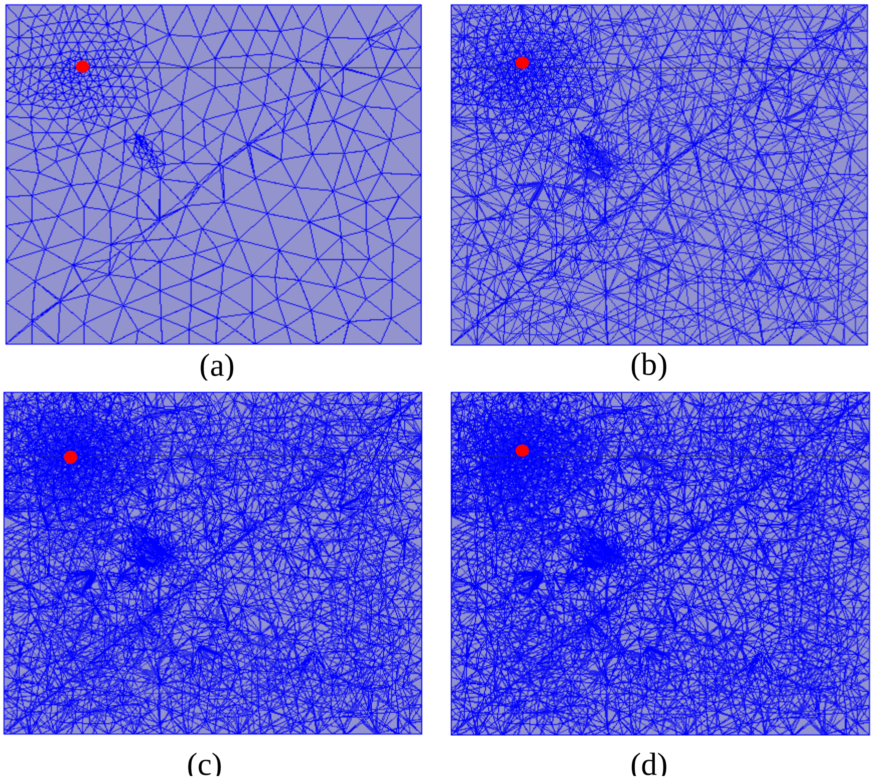

Figure 3.23: HFSS tissue model #4 tetrahedra mesh showing a raster location. (a) Top boundary of domain, (b) 140 μm above tissue, (c) 5 μm above tissue, (d) top of tissue.

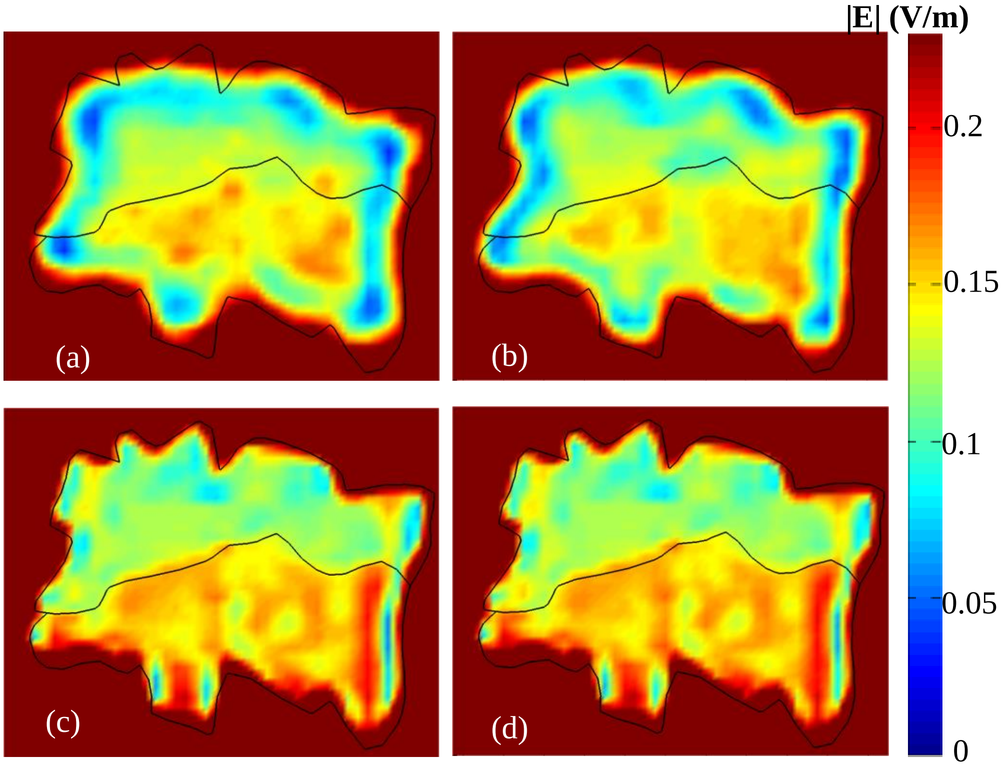

Figure 3.24: HFSS tissue model #4 simulated images at different planes. (a) Top boundary of domain, (b) 140 μm above tissue, (c) 5 μm above tissue, (d) top of tissue.

The image of the HFSS tissue model obtained at the surface of the tissue and at 5 µm away from the tissue surface showed significant reduction in the artifact low field border surrounding the tissue regions. However, the artifact border still appears in some part of the image as shown in Fig. 3.24c and Fig. 3.24d. A comparison of the images of the tissue models obtained at the top boundary and at the surface of the tissue model is shown in Fig. 3.25 through Fig. 3.28. The error (dE) versus the adaptive pass is also shown for the first raster location of the Gaussian beam. The image of the tissue models at the surface of the tissue show significant reduction of the low field border surrounding the tissue regions of the models (see Fig. 3.25 – Fig. 3.28).

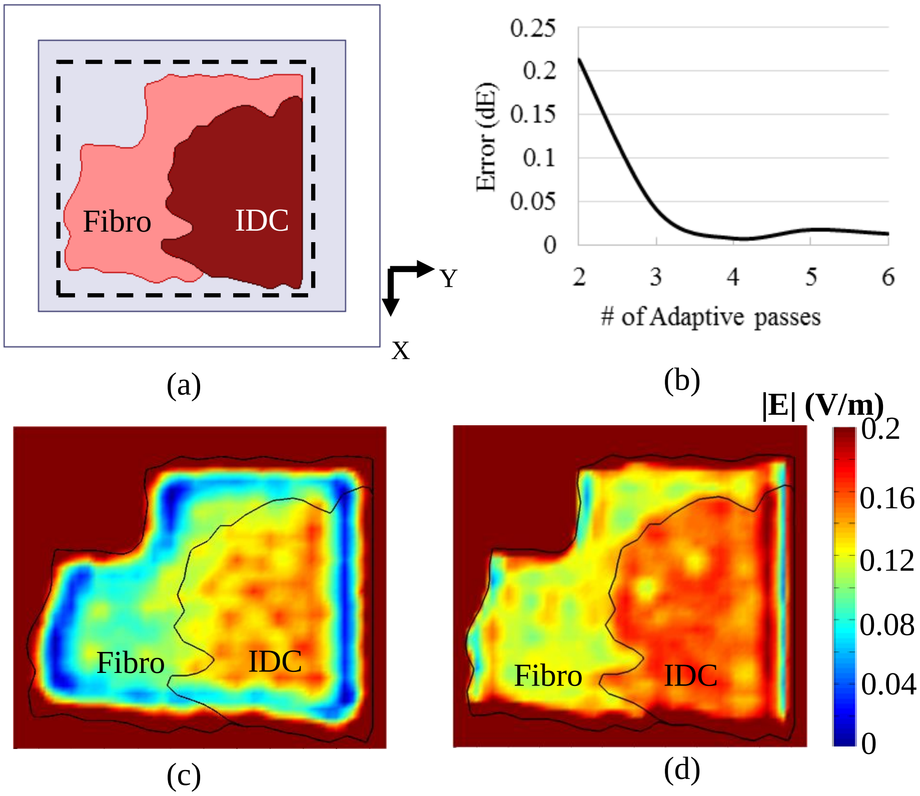

(a) (b)

(c) (d)

Figure 3.25: HFSS tissue model #1. (a) Top view of model showing imaged area (a) convergence curve (c) image at top boundary of domain (d) image at surface of the tissue.

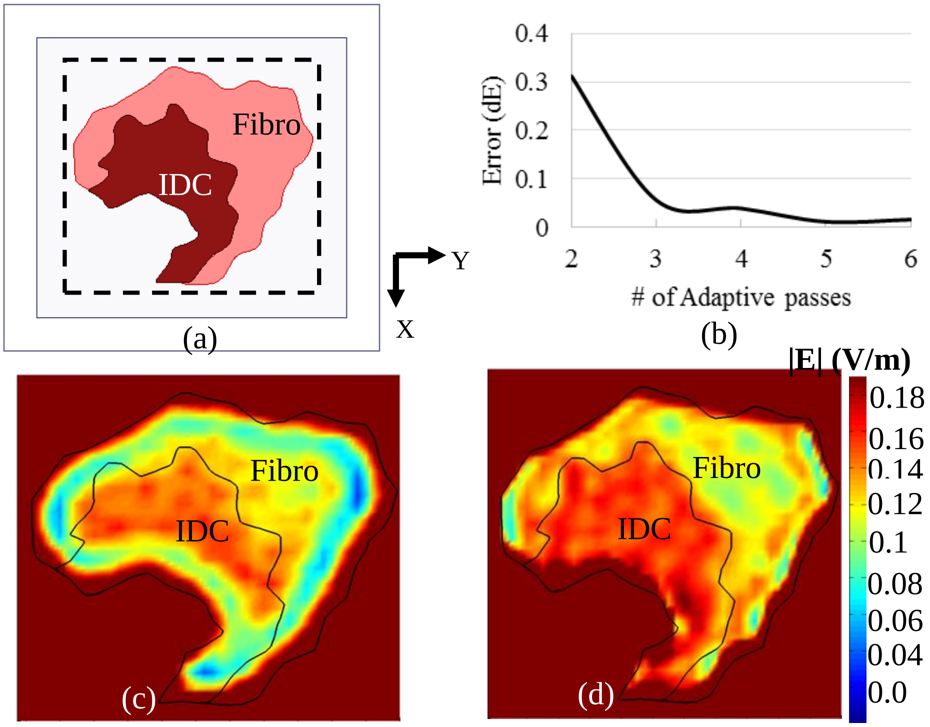

Figure 3.26: HFSS tissue model #2. (a) Top view of model showing imaged area, (a) convergence curve, (c) image at top boundary of domain, (d) image at surface of the tissue.

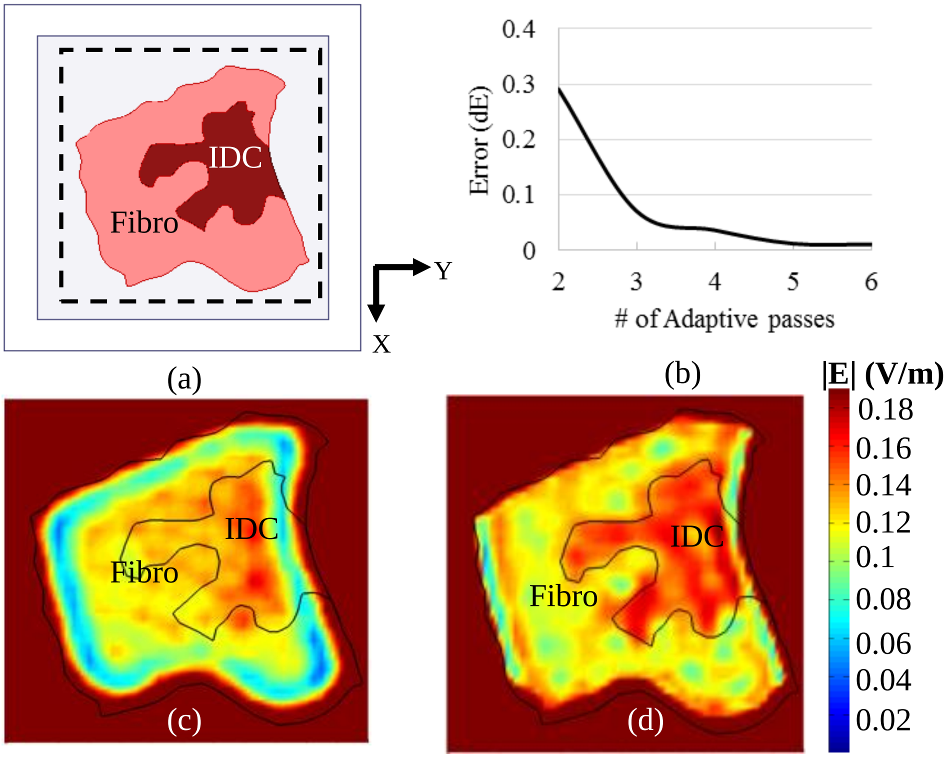

Figure 3.27 : HFSS tissue model #3. (a) Top view of model showing imaged area, (a) convergence curve, (c) image at top boundary of domain, (d) image at surface of the tissue.

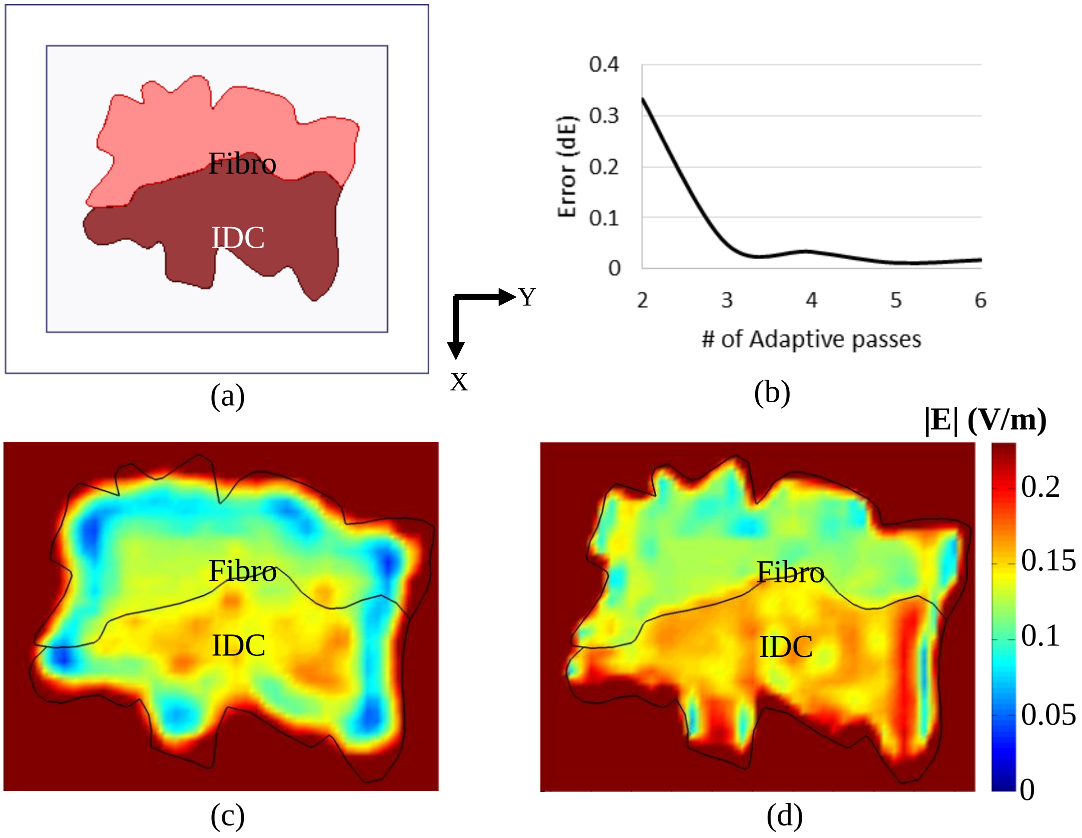

(a) (b) (c) (d)

Figure 3.28: HFSS tissue model #4 (a) Top view of model showing imaged area, (a) convergence curve, (c) image at top boundary of domain, (d) image at surface of the tissue.

The low field border still appears along parts of the tissue model that are tangential or almost tangential to the x-axis. At the surface of the tissue, the black outline that represents the shape of the tissue matches the image created in all models better that the images created at the top boundary. The images obtained at the tissue surface give better representation of the HFSS tissue models than images obtained at the top boundary of the computational domain.

3.4 Alternative Approach of Creating Tissue Model Images

Further investigation was carried out to ascertain the cause of the artifact low field region bordering some parts of the tissue models simulated in HFSS. Another approach of creating the images was investigated, as it was thought that the low field borders could be as a result of the averaging of field over pixels used for creating all previous images. In this new approach, a vector addition of fields on the plane that the image was to be viewed was conducted for all the raster locations of the incident beam in the model. The images created this way are shown Fig. 3.29 and Fig. 3.30 for the HFSS tissue models #2 and #4, respectively. The images were obtained at the surface of the tissue.

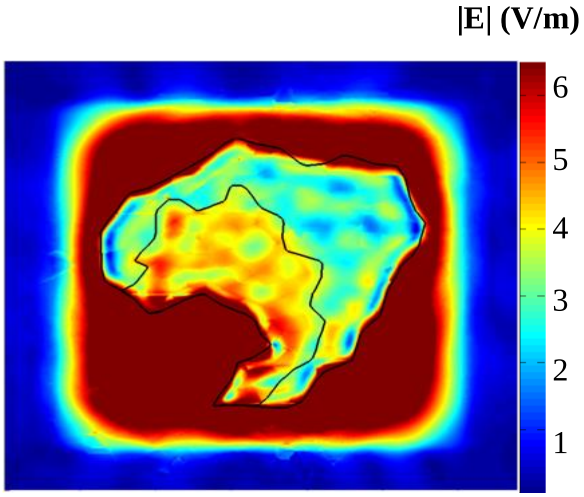

Figure 3.29: Simulated image created at top of tissue by adding field at for all raster locations of beam for HSSF tissue model #2. Gaussian beam scanned in 100 µm steps.

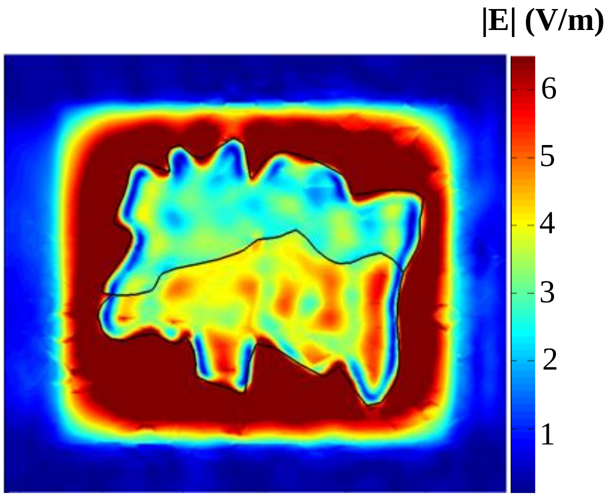

Figure 3.30: Simulated image created at top of tissue by adding field at for all raster locations of beam for HFSS tissue Model #4. Gaussian beam scanned in 100 µm steps.

The images created by adding field vectors from all raster location (see Fig. 3.29 and Fig. 3.30) produces images of the model tissues that are similar to those created by averaging field within pixel associated with each raster location (see Fig. 3.26 and Fig. 3.28). Also, the border of low field surrounding the tissue regions of the model was observed for both image generation approaches.

3.5 Images of Tissue Model Embedded in Paraffin

In the THz experimental work of this research, the cancer tissue samples were embedded in paraffin. As a way to understand the reason for the artifact low field border around images, a modification was made to the simulation by surrounding the tissue model with paraffin. Before simulating the entire tissue model surrounded by paraffin, a small square area of 600 µm x 600 µm of tissue model #4 was first simulated. The square areas was made up of 36 raster locations where the Gaussian beam was incident. Fig. 3.31 shows HFSS tissue model #4 with the imaged area shown as the dashed line square.

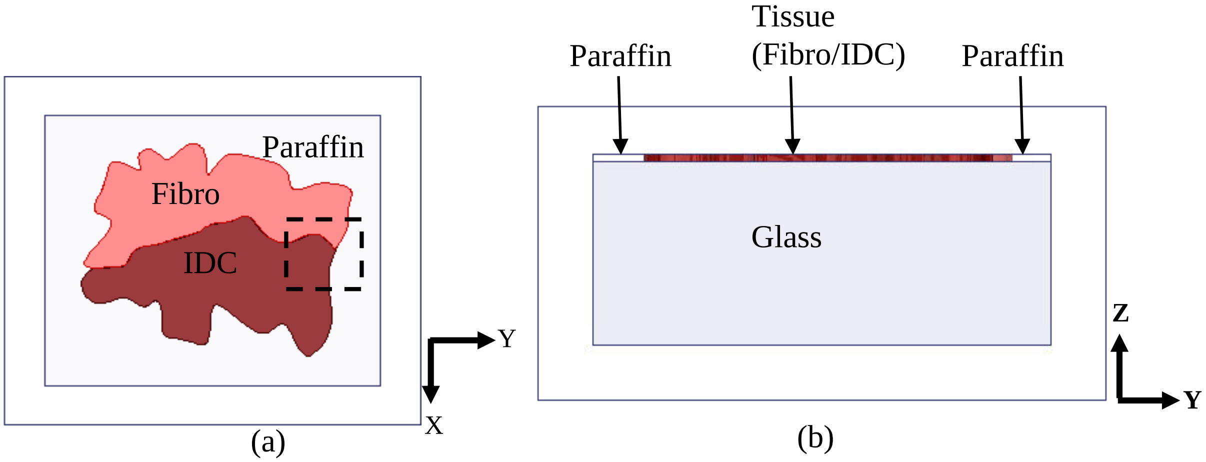

Figure 3.31: HFSS tissue model #4 embedded in paraffin. (a) Top view, (b) y-z cross-section.

The simulated image of the square area of the model obtained by vector summation of the electric fields due to all raster locations at the surface of tissue is shown in Fig. 3.32. Fig. 3.32a shows the image of the model when the tissue was surrounded by air and Fig. 3.32b shows the image when it was surrounded by paraffin.

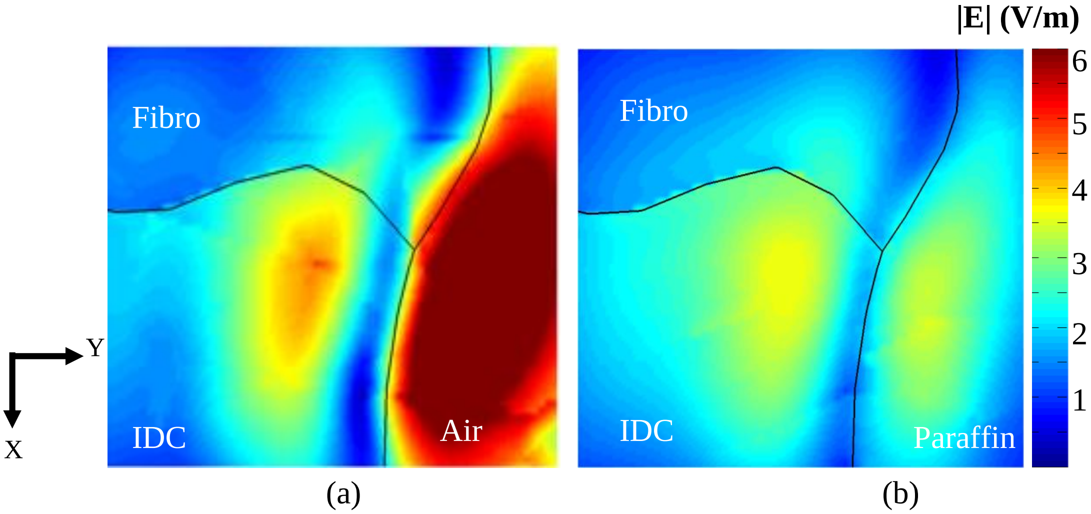

Figure 3.32: Simulated square area of HFSS tissue model #4. (a) Tissue surrounded by air (b) tissue embedded in paraffin.

The tissue model surrounded by paraffin produced a better image, having smaller artifact low field region around the tissue when compared to the model having the tissue surrounded by air. It can be inferred that the border surrounding the tissue region could be as a result of the difference in regions experienced as waves in the tissue propagate along the y-axis towards the boundary of the tissue and surrounding region (air or paraffin). Some of those waves would be reflected at this boundary into the tissue region due to the difference in the regions. The reflected field from the boundary can interfere constructively or destructively with the incident field within the tissue region to produce standing waves. Standing waves are produced when waves travelling in opposite directions within a region interfere to produce a sinusoidal pattern of the total field amplitude. The maximum total field amplitude occurs when the two waves travelling in opposite directions interfere constructively, and the minimum total field amplitude occur when the waves interfere destructively.

In order to confirm that the low field borders around the tissue were a result of standing waves, two cases of regions surrounding the tissue were investigated. In the first case, the tissue region of the HFSS model was surrounded with a region having the same properties as Fibro regions of the tissue (IDC and fibro), while the second case has IDC region surrounding the tissue (see Fig. 3.33).

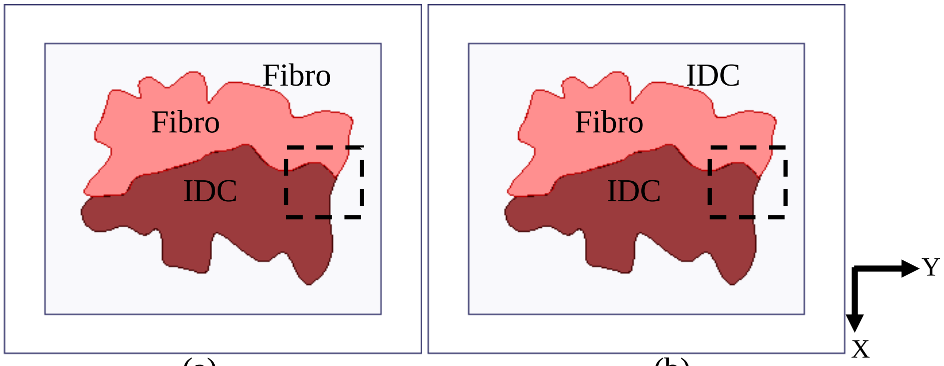

(a) (b)

Figure 3.33: HFSS tissue model #4. (a) Embedded in fibro region, (b) embedded in IDC region.

It was expected that there would be no border of low field next to the fibro region when the tissue was surrounded with fibro, and the same was expected of the IDC region when tissue was surrounded by IDC. The results were as expected (see Fig. 3.34), and confirms that the borders of low field around the tissue was caused by the mismatch in regions at the boundary of the tissue and air (or paraffin).

Figure 3.34 shows the comparison of the square region imaged in HFSS tissue model #4 for different materials surrounding the tissue. Fig. 3.34a shows the image when the tissue region was surrounded by air and it had the largest low field boundary surrounding the tissue when compared to other images of Fig. 3.34. Fig. 3.34b shows the image obtained when tissue region was surrounded by paraffin, and it has smaller low-field region around the tissue compared to Fig3.34a. Fig. 3.34c and Fig. 3.34d had no low-field boundary surrounding the tissue regions.

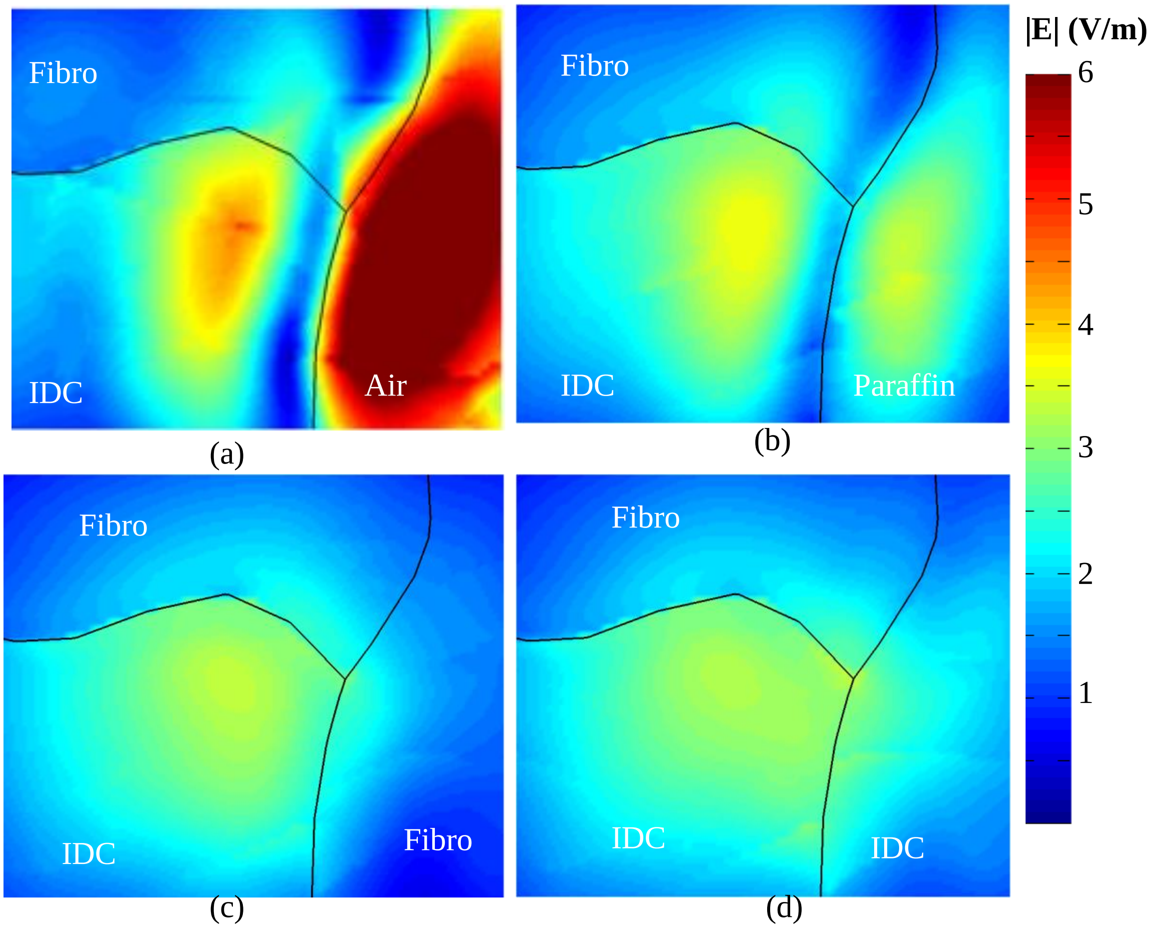

(a) (b) (c) (d)

Figure 3.34: HFSS simulated image of square area of tissue model #4. (a) Tissues surrounded by air, (b) tissue embedded in paraffin, (c) tissue embedded in fibro region, (d) tissue embedded in IDC region.

A full image of HFSS tissue model #4 was simulated with paraffin surrounding the tissue region. A comparison of the simulated image of the model when tissue region was surrounded by air and paraffin is presented in Fig. 3.35. From Fig. 3.35, the model with the tissue embedded in paraffin reflected lower E-field from the paraffin region compared to the model with the tissue surrounded by air. Also, the artifact low field region surrounding the tissue region reduced when the tissue model was embedded in paraffin.

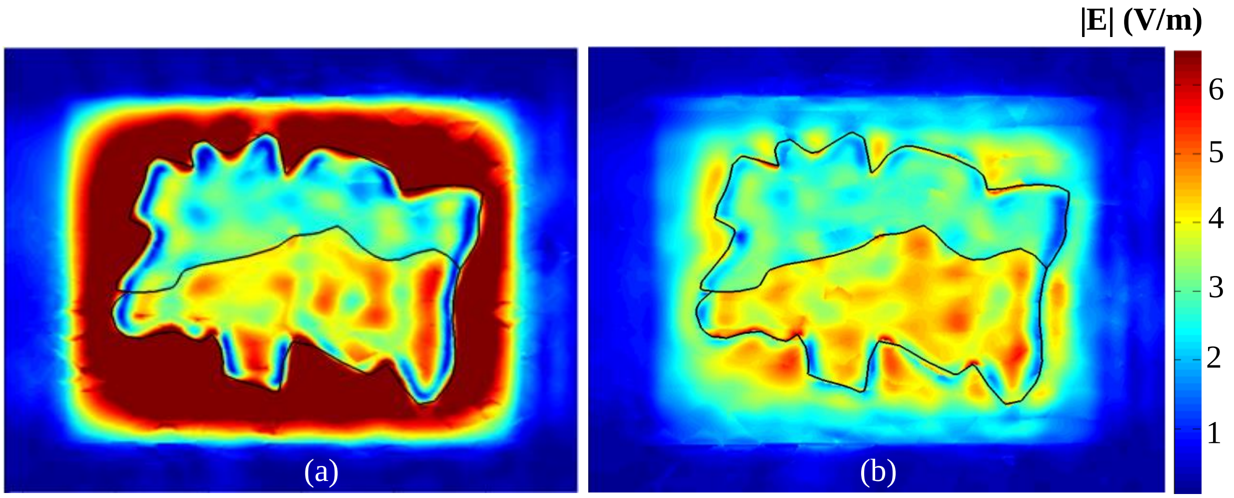

Figure 3.35: Simulated HFSS image for tissue model #4 obtained at surface of tissue. (a) Tissue surrounded by air, (b) tissue embedded in paraffin.

3.6 HFSS Parametric Setup Effect on the Simulation Images

In the parametric set-up used in simulating the raster scanning in HFSS, there was an important setting that affects the images simulated in HFSS. There is an option to ‘copy geometrically equivalent meshes’ as the Gaussian beam is raster scanned across the area to be images, (see Fig. 3.36). This option did not regenerate a new mesh for the simulation as the Gaussian beam was scanned across the tissue model, instead it used the mesh from the previous raster location to compute fields for the new location.

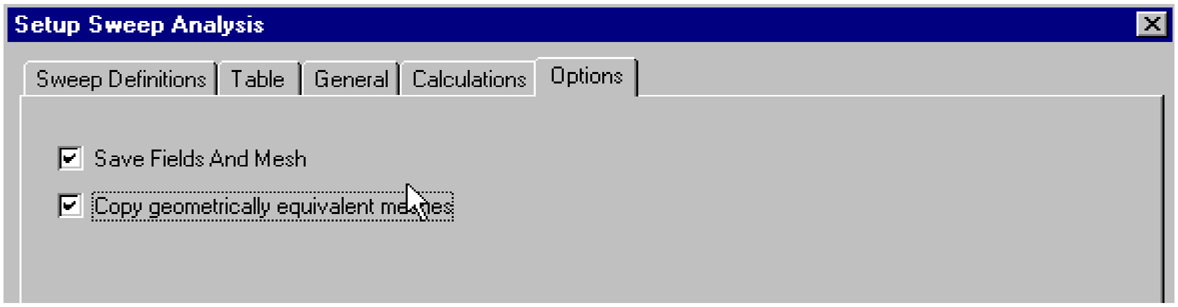

☑ Save Fields And Mesh

☑ Copy geometrically equivalent meshes

Figure 3.36: HFSS parametric setup options.

Selecting this option made the simulation faster compared with the case when it was not selected. However, the field solutions were not as accurate as when the option was not selected. For the simulations presented so far, the HFSS set-up was conducted by selecting the option of 'copy geometrically equivalent meshes' to handle the large computational size of the problem. HFSS tissue model #4 embedded in paraffin was simulated without selecting the option of 'copy geometrically equivalent mesh' and the simulated image was compared to when the option was selected as shown in Fig. 3.37.

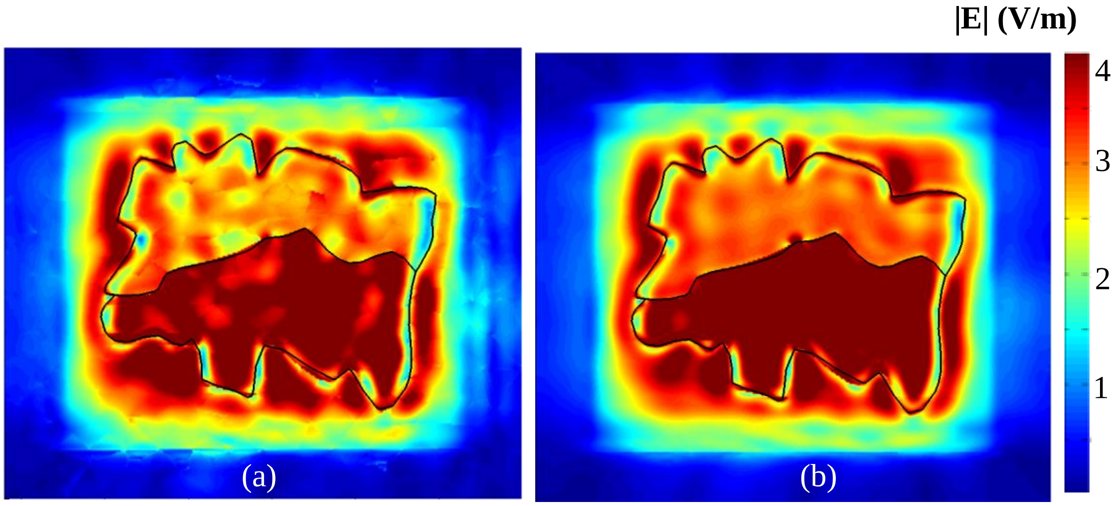

Figure 3.37: HFSS Tissue Model #4 embedded in paraffin. (a) Selecting the option to copy geometrically equivalent mesh, (b) no selecting the option.

The image obtained by not selecting the option of copying mesh was better than the image obtained when the option of copying mesh was selected. This was expected as the mesh for the computational domain was generated for each raster location of the Gaussian beam if the option was not selected. This advantage, however, comes at the expense of increased simulation time.

3.7 Simulation of THz Imaging using a Single Gaussian Beam

One of the limitations of the THz time-domain pulsed system is its reliance on raster scanning which reduces how fast an image can be acquired [32]. Terahertz cameras that can provide real time images are now commercially available [33]. In this research, a preliminary investigation into THz imaging using the concept of THz camera was conducted. HFSS tissue model #4 embedded in paraffin was imaged using a single Gaussian beam focused at the center of the tissue (marked by x in Fig. 3.38). Three Gaussian beam widths: 5000 µm, 2800 µm, 1400 µm, were used in the simulation.

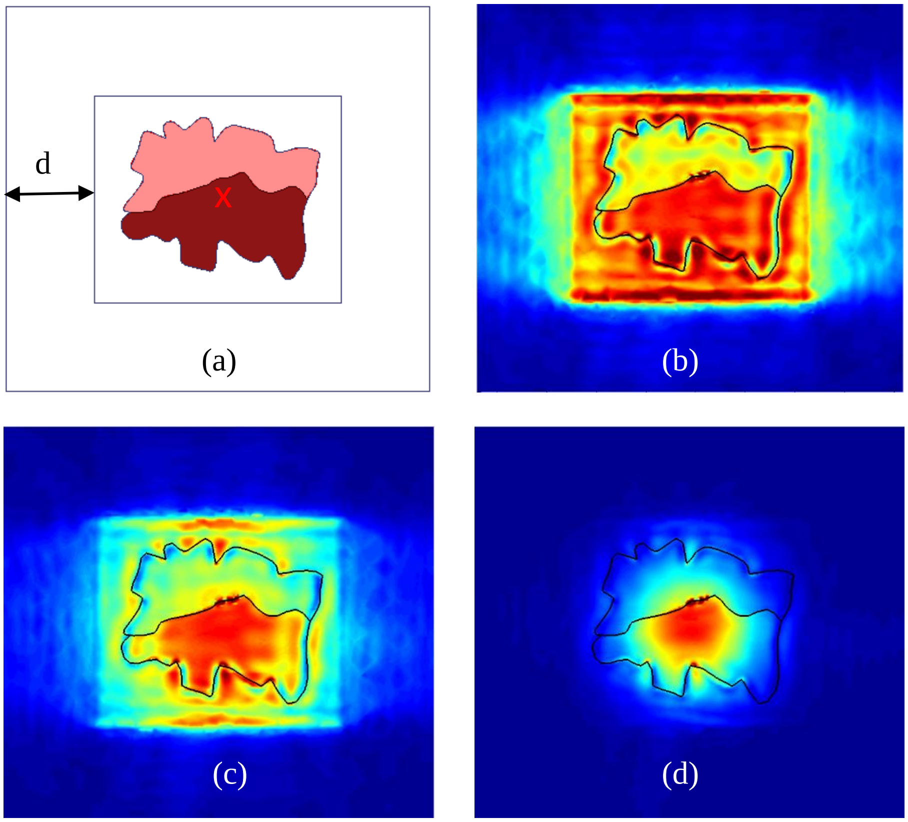

Figure 3.38: THz camera imaging simulation of model tissue #4 embedded in Paraffin. (a) HFSS model, (b) image using beam width of 5000 µm, (c) image using beam width of 2800 µm, (d) image using beam width of 1400 µm.

The images were created by observing the scattered E-field on the plane at the tissue surface. The distance, d, between the problem domain and the surrounding PML was set to 800 µm to prevent field reflections from the PML. However, as shown in Fig. 3.38b and Fig. 3.38c, some reflections were observed from the PML for the 5000 µm, and 2800 µm Gaussian beam widths simulations. The THz camera idea will be further investigated for future publication.

4. Conclusions and Future Work

4.1 Conclusions

This work has successfully developed a methodology for numerical simulation of THz reflection imaging using HFSS. It also validated the trend of the experimental results obtained from the time domain pulsed THz system (TPS) images of formalin-fixed paraffin embedded excised tissue sections, conducted by other researchers in the group. The simulated images showed good correlation with pathology images that were modeled using the HFSS package.

Similar to results obtained from the experimental measurements, thicker tissue sections model provided better differentiation between the Infiltrating Ductal Carcinoma (IDC), and Fibro glandular (Fibro) regions. The 40 µm-thick tissue models provided a better differentiation between these regions compared with the 10 µm-thick tissue. Also, scanning the incident Gaussian beam over the tissue section configuration using smaller step sizes provided better simulated images. Using a step size of 100 µm in scanning the Gaussian beam over the model gave a better image compared with the images obtained with scanning with 200 µm steps. This can be explained by the fact that scanning in100 µm steps provides more field data compared with the 200 µm steps.

Regarding using the HFSS for simulating the images of breast cancer sections, several parameters were found to have significant effect on the accuracy of these simulations. The tetrahedral mesh refinement in HFSS at the plane where simulated images were observed was found to be crucial in obtaining accurate images. Artifacts of low field regions surrounding the tissue were observed in the images when the tetrahedral mesh was not well refined at the receiving plane in the far field. The results showed that simulating the images in the near field zone provided better images of these tissues compared with those obtained in the far field zone inside the computational domain. This can be explained by the fact that tetrahedral meshes close to the tissue surface were better refined when compared to meshes at the PML boundary. The better refined meshes at the tissue surface ensured better accuracy of field solution than the less refined meshes at the PML boundary. Also, better images were obtained when the structure was discretized individually at each raster location of the incident Gaussian beam compared with when the same discretization was used for all raster scans. This option can be selected from the HFSS set-up parameters.

The simulated THz images of the tissue using a single Gaussian beam that illuminates the whole structure provided a good agreement with the raster scanning approach. The approach can be further investigated in the future and has potential to provide a methodology for imaging cancer tissues.

4.2 Future Work

This work focused on simulating THz reflection imaging mode. The THz transmission imaging mode could follow the simulation methodology developed in this thesis. In that case, glass slides would not be used but polystyrene slides would be more appropriate as described in Section 2.1.1. This future simulation would help understand the experimental images of THz transmission mode of breast cancer tissue samples.

For the reflection imaging simulation conducted in this research, further investigation into the effect of other tissue thicknesses would be helpful to better understand the effect of tissue thickness on the ability of THz for differentiating between cancer and non-cancer tissue regions. Also, finer tetrahedral mesh could be investigated for all tissue models in the future. Finally, a time domain simulation package could be investigated to produce THz images in the time domain similar to the Pulsed Time Domain THz system available in the lab. In this direction, images of the 3D tumor could be investigated versus planar sections studied in the current work.

References

[1] C. Jansen, S. Wietzke, O. Peters, M. Scheller, N. Vieweg, M. Salhi, N. Krumbholz, C. Jördens, T. Hochrein, and M. Koch, “Terahertz imaging: applications and perspectives,” *Appl. Opt.*, vol. 49, no. 19, pp. E48–E57, 2010.

[2] T. Bowman, M. El-Shenawee, and S. G. Sharma, “Terahertz spectroscopy for the characterization of excised human breast tissue,” in *Microwave Symposium (IMS), IEEE MTT-S International*, 2014.

[3] R. M. Woodward, V. P. Wallace, D. D. Arnone, E. H. Linfield, and M. Pepper, “Terahertz pulsed imaging of skin cancer in the time and frequency domain,” *J. Biol. Phys.*, vol. 29, no. 2–3, pp. 257–259, 2003.

[4] S. J. Oh, J. Kang, I. Maeng, J.-S. Suh, Y.-M. Huh, S. Haam, and J.-H. Son, “Nanoparticle-enabled terahertz imaging for cancer diagnosis,” *Opt. Express*, vol. 17, no. 5, pp. 3469–3475, 2009.

[5] S. Nakajima, H. Hoshina, M. Yamashita, C. Otani, and N. Miyoshi, “Terahertz imaging diagnostics of cancer tissues with a chemometrics technique,” *Appl. Phys. Lett.*, vol. 90, no. 4, p. 041102, 2007.

[6] A. J. Fitzgerald, V. P. Wallace, M. Jimenez-Linan, L. Bobrow, R. J. Pye, A. D. Purushotham, and D. D. Arnone, “Terahertz pulsed imaging of human breast tumors 1,” *Radiology*, vol. 239, no. 2, pp. 533–540, 2006.

[7] D. Crawley, C. Longbottom, V. P. Wallace, B. Cole, D. Arnone, and M. Pepper, “Three-dimensional terahertz pulse imaging of dental tissue,” *J. Biomed. Opt.*, vol. 8, no. 2, pp. 303–307, 2003.

[8] Z. D. Taylor, J. Garritano, S. Sung, N. Bajwa, D. B. Bennett, B. Nowroozi, P. Tewari, J. Sayre, J.-P. Hubschman, S. Deng, E. R. Brown, and W. S. Grundfest, “THz and mm-Wave Sensing of Corneal Tissue Water Content: Electromagnetic Modeling and Analysis,” *IEEE Trans. Terahertz Sci. Technol.*, vol. 5, no. 2, pp. 170–183, Mar. 2015.

[9] K. Humphreys, J. P. Loughran, M. Gradziel, W. Lanigan, T. Ward, J. A. Murphy, and C. O’Sullivan, “Medical applications of terahertz imaging: a review of current technology and potential applications in biomedical engineering,” in *Engineering in Medicine and Biology Society, 2004. IEMBS’04. 26th Annual International Conference of the IEEE*, 2004, vol. 1, pp. 1302–1305.

[10] M.-A. Brun, F. Formanek, A. Yasuda, M. Sekine, N. Ando, and Y. Eishii, “Terahertz imaging applied to cancer diagnosis,” *Phys. Med. Biol.*, vol. 55, no. 16, pp. 4615–4623, Aug. 2010.

[11] N. Palka, “Identification of concealed materials, including explosives, by terahertz reflection spectroscopy,” *Opt. Eng.*, vol. 53, no. 3, pp. 031202–031202, 2014.

[12] S. Wietzke, C. Jördens, N. Krumbholz, B. Baudrit, M. Bastian, and M. Koch, “Terahertz imaging: a new non-destructive technique for the quality control of plastic weld joints,” *J. Eur. Opt. Soc.-Rapid Publ.*, vol. 2, 2007.

[13] T. C. Bowman, “Experimental Terahertz Imaging and Spectroscopy of Ex-vivo Breast Cancer Tissue,” *MS Thesis Dept Elect Eng Univ Ark.*, 2014.

[14] T. Bowman, M. El-Shenawee, and L. Campbell, “Terahertz Imaging of Excised Breast Tumor Tissue on Paraffin Sections,” *IEEE Trans. Antennas Propagation*, pp. 2088–2097, 2015.

[15] N. M. Burford, M. O. El-Shenawee, C. B. O’neal, and K. J. Olejniczak, “Terahertz Imaging for Nondestructive Evaluation of Packaged Power Electronic Devices.” in *International Journal of Emerging Technology and Advanced Engineering*, vol. 4, no. 1, pp. 395-401, 2014.

[16] N. M. Burford, B. Freiburger, and M. El-Shenawee, “Terahertz investigation of X-ray anti-imaging coatings: Spectroscopic characterization and imaging,” in *Infrared, Millimeter, and Terahertz waves (IRMMW-THz), 2014 39th International Conference*, 2014.

[17] E. L. Jacobs, S. Moyer, C. C. Franck, F. C. DeLucia, C. Casto, D. T. Petkie, S. R. Murrill, and C. E. Halford, “Concealed weapon identification using terahertz imaging sensors.,” in *Defense and Security Symposium. International Society for Optics and Photonics*, p. 62120J–62120J–10, 2006.

[18] M. J. Fitch and R. Osiander, “Terahertz waves for communications and sensing,” *Johns Hopkins APL Tech. Dig.*, vol. 25, no. 4, pp. 348–355, 2004.

[19] C. Yu, S. Fan, Y. Sun, and E. Pickwell-MacPherson, “The potential of terahertz imaging for cancer diagnosis: A review of investigations to date,” *Quant. Imaging Med. Surg.*, vol. 2, no. 1, p. 33, 2012.

[20] E. Episkopou, S. Papantonis, W. J. Otter, and S. Lucyszyn, “Defining Material Parameters in Commercial EM Solvers for Arbitrary Metal-Based THz Structures,” *IEEE Trans. Terahertz Sci. Technol.*, vol. 2, no. 5, pp. 513–524, Sep. 2012.

[21] C. D. Nordquist, M. C. Wanke, A. M. Rowen, C. L. Arrington, M. Lee, and A. D. Grine, “Design, fabrication, and characterization of metal micromachined rectangular waveguides at 3 THz,” in *Antennas and Propagation Society International Symposium, 2008. AP-S 2008. IEEE*, 2008.

[22] D. Sanchez-Escuderos, M. Ferrando-Bataller, M. Baquero-Escudero, and J. I. Herranz, “Ebg structures for antenna design at THz frequencies,” in *Antennas and Propagation (APSURSI), 2011 IEEE International Symposium on*, pp. 1824–1827, 2011.

[23] W. Miao, Y. Delorme, F. Dauplay, G. Beaudin, Q. J. Yao, and S. C. Shi, “Simulation of an integrated log-spiral antenna at terahertz,” in *Antennas, Propagation and EM Theory, 2008. ISAPE 2008. 8th International Symposium on*, pp. 58–61, 2008.

[24] B. B. Hu and M. C. Nuss, “Imaging with terahertz waves,” *Opt. Lett.*, vol. 20, no. 16, pp. 1716–1718, 1995.

[25] K. Kawase, Y. Ogawa, Y. Watanabe, and H. Inoue, “Non-destructive terahertz imaging of illicit drugs using spectral fingerprints,” *Opt. Express*, vol. 11, no. 20, pp. 2549–2554, 2003.

[26] T. Bowman, A. M. Hassan, and M. O. El-Shenawee, “Terahertz Imaging of breast cancer Margin using Linear Sampling Method,” in *Antennas and Propagation Society International Symposium (APSURSI), 2013 IEEE*, pp. 538 – 539, 2013.

[27] T. C. Bowman, A. M. Hassan, and M. El-Shenawee, “Imaging 2D Breast Cancer Tumor Margin at Terahertz Frequency using Numerical Field Data based on DDSCAT.,” *Appl. Comput. Electromagn. Soc. J.*, vol. 28, no. 11, 2013.

[28] A. M. Hassan, D. C. Hufnagle, M. El-Shenawee, and G. E. Pacey, “Terahertz imaging for margin assessment of breast cancer tumors,” in *Microwave Symposium Digest (MTT), IEEE MTT-S International*, 2012.

[29] “Teraview.” [Online]. Available: http://www.teraview.com/. [Accessed: 16-Apr-2015].

[30] “ANSYS HFSS.” [Online]. Available: http://www.ansys.com/Products/Simulation+Technology/Electronics/Signal+Integrity/ch.ANSYS+HFSS.cz. [Accessed: 16-Apr-2015].

[31] “Arkansas High Performance Computing Center.” [Online]. Available: http://hpc.uark.edu/hpc/resources/hardware.html. [Accessed: 16-Apr-2015].

[32] W. L. Chan, J. Deibel, and D. M. Mittleman, “Imaging with terahertz radiation,” *Rep. Prog. Phys.*, vol. 70, no. 8, pp. 1325–1379, Aug. 2007.

[33] “Traycer.” [Online]. Available: http://www.traycer.com/. [Accessed: 18-Apr-2015].

Appendix A: Description of Research for Popular Publication

Alternative Way of Exploring the ‘THz gap’ for Biomedical Imaging

By Abayomi Omolewu

The terahertz region of the electromagnetic spectrum has gained much attention in the past decades and researcher are exploring this region of the electromagnetic spectrum for applications in communication, electronics, security and biomedical imaging. Most research in the field required acquiring terahertz systems, and the most popular of these systems is the terahertz time pulsed spectroscopy system. Current terahertz systems used for exploring the terahertz region of the electromagnetic spectrum are expensive and few of them are available for researches to make use of.

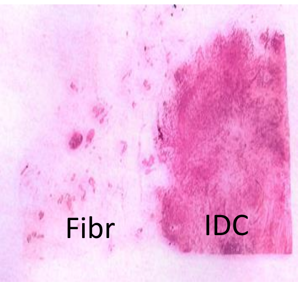

Pathology image

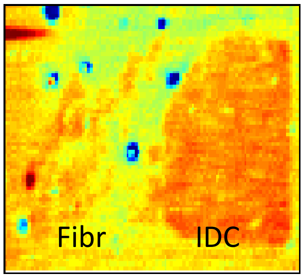

Experimental image from THz TPS Spectra 3000

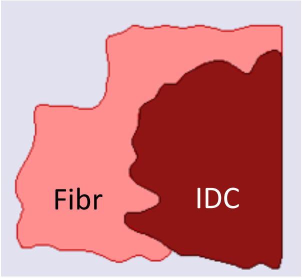

HFSS simulated

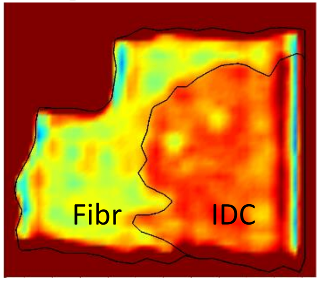

HFSS simulated image at 1THz

A group of researchers headed by Dr. Magda El-Shenawee of Electrical Engineering at the University of Arkansas have employed another approach of probing the terahertz region of the electromagnetic spectrum. The group that has been known for its work on terahertz imaging for breast cancer application use one of the available commercial electromagnetic solver packages to reproduce some of it experimental results (shown in figure). The researchers employed the ANSYS High Frequency Structural Simulator to validate experimental results of terahertz imaging flat sections of breast cancer tissue. This approach of using a software is convenient alternative to acquiring an expensive terahertz system for terahertz imaging. It also helped the researched understand how terahertz radiation interacts with biological tissue.

With breast cancer being the highest cause of death among women, the researchers believe that this computation approach to breast cancer imaging will provide a different and in-depth analysis of breast cancer margins. The insight gained from this research will help prevent breast cancer reoccurrence for women that have undergone lumpectomy and help reduce the number of women that will need to undergo mastectomy due to breast cancer reoccurrence.

Knowledge gained from this research could also help reduce the emotional and financial burdens that breast cancer patients and their families go through due to cancer reoccurrence after a lumpectomy. With the better accuracy envisioned for terahertz imaging for cancer diagnosis, it is expected that this research will help prevent the need of second surgery for breast cancer patients which can be financially and emotionally burdensome.

Researchers believe that this new method of investigating terahertz imaging for breast cancer imaging will give insight into the interaction of terahertz radiation with cancer tissue and bring relief to breast cancer patients in the near future.

Appendix B: Executive Summary of Newly Created Intellectual Property

There was no intellectual property created from this research.

Appendix C: Potential Patent and Commercialization Aspect of Items found in Appendix B

There were no potential patents and commercialization aspects from this research.

Appendix D: Broader Impact

D.1. Applicability of Research Methods to Other Problems

The methodology developed in this research can be employed in other terahertz imaging applications. With many materials having unique spectral fingerprints and the availability of databases of material properties at terahertz frequencies, other imaging applications can be investigated using the method developed in this research.

One of the potential applications of the methodology developed in this research is national security. A preventive security measure that involves terahertz imaging simulation of dangerous substances and materials can be done with a view to identifying these substances before they develop into security threats. By using the methodology in this research, a database of the terahertz signatures of these dangerous substances and materials can be maintain and used to avert security breaches that could occur in future.

D.2. Impact of Research Results on U.S. and Global Society

The images obtained from this research has proven that terahertz imaging can be done using available electromagnetic software. Employing this approach can help improve national security by helping with screening at airports, and other public places. Terahertz imaging simulations of dangerous materials and chemical can be done to understand how they interact with terahertz radiation. This prior knowledge can help in putting the necessary precautions to prevent security threats that could arise from these materials and chemicals. As an example, improvised explosives could be imaged through the simulation methods developed in this research and results obtained could help prevent their use by terrorists and other ill-intentioned individuals.

D.3. Impact of Research on the Environment

This research does not have a direct impact on the environment. However, relying more of simulations for some research that would ordinarily require a terahertz systems can reduce the amount of energy used. This energy savings can help reduce the carbon foot print in the environment.

Appendix E: Microsoft Project for MS MicroEp Degree Plan

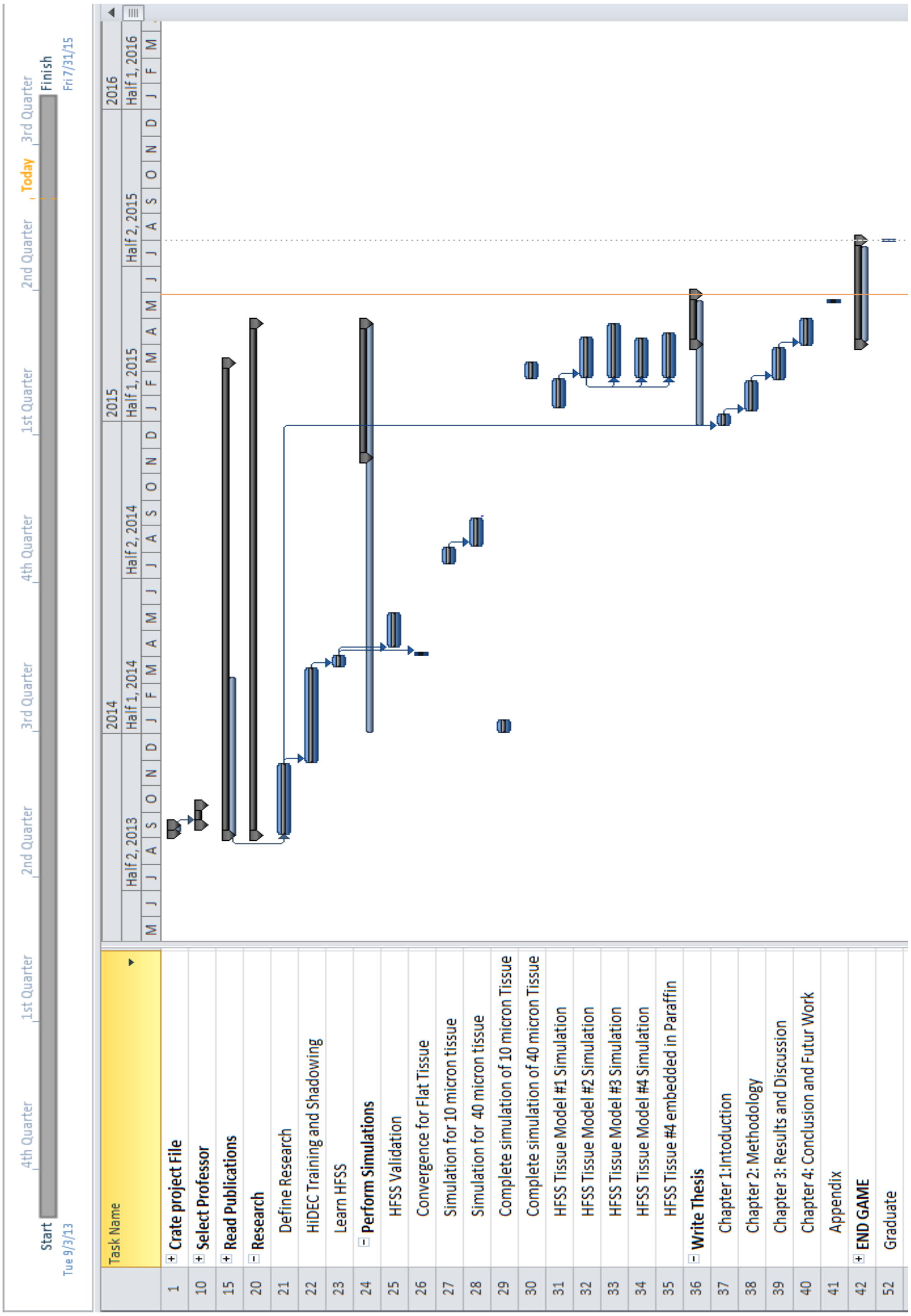

	Task Name
1	⊞ **Crate project File**
10	⊞ **Select Professor**
15	⊞ **Read Publications**
20	⊟ **Research**
21	Define Research
22	HiDEC Training and Shadowing
23	Learn HFSS
24	⊟ **Perform Simulations**
25	HFSS Validation
26	Convergence for Flat Tissue
27	Simulation for 10 micron tissue
28	Simulation for 40 micron tissue
29	Complete simulation of 10 micron Tissue
30	Complete simulation of 40 micron Tissue
31	HFSS Tissue Model #1 Simulation
32	HFSS Tissue Model #2 Simulation
33	HFSS Tissue Model #3 Simulation
34	HFSS Tissue Model #4 Simulation
35	HFSS Tissue #4 embedded in Paraffin
36	⊟ **Write Thesis**
37	Chapter 1:Intoduction
38	Chapter 2: Methodology
39	Chapter 3: Results and Discussion
40	Chapter 4: Conclusion and Futur Work
41	Appendix
42	⊞ **END GAME**
52	Graduate

Appendix F: Identification of All Software used in Research and Thesis Generation

Computer #1:
  Model Number: N/A
  Computer Name: eleg-r4906w06.uark.edu
  Location: ENRC 4906
  Owner: Dr. Magda El-Shenawee
Software #1:
  Name: ANSYS® HFSS
  Owner: Dr. Magda El-Shenawee
  Serial Number: 1-228293401
Software #2:
  Name: Microsoft Office 2013
  Owner: Electrical Engineering Department
Software #3:
  Name: MATLAB R2013a (8.1.0.604)
  Owner: Electrical Engineering Department
  License Number: 601103

Appendix G: Publications- Published, Submitted, and Planned

Conference Proceedings

- A. O. Omolewu, T. C. Bowman, and M. O. El-Shenawee, “Numerical Simulation of THz Reflection Imaging of Breast Cancer Tissue,” 2015 IEEE AP-S Symposium on Antennas and Propagation and URSI CNC/USNC Joint Meeting, Vancouver, BC, Canada, 2015. (Accepted for presentation.)